

Distribution Agreement

In presenting this thesis or dissertation as a partial fulfillment of the requirements for an advanced degree from Emory University, I hereby grant to Emory University and its agents the non-exclusive license to archive, make accessible, and display my thesis or dissertation in whole or in part in all forms of media, now or hereafter known, including display on the world wide web. I understand that I may select some access restrictions as part of the online submission of this thesis or dissertation. I retain all ownership rights to the copyright of the thesis or dissertation. I also retain the right to use in future works (such as articles or books) all or part of this thesis or dissertation.

Signature:

Xiaotong Chen

Date

Single Photons, Phonons and Valley-Locked Spins in Atomically
Thin WSe₂

by

Xiaotong Chen
Doctor of Philosophy

Physics Department

Ajit Srivastava, Ph.D.
Advisor

Hayk Harutyunyan, Ph.D.
Committee Member

Sergei Urazhdin, Ph.D.
Committee Member

Justin Burton, Ph.D.
Committee Member

Tianquan Lian, Ph. D.
Committee Member

Accepted:

Lisa A. Tedesco, Ph.D.
Dean of the James T. Laney School of Graduate Studies

Date

Single Photons, Phonons and Valley-Locked Spins in Atomically
Thin WSe₂

by

Xiaotong Chen
B.S., Shandong University, P.R. China, 2015

Advisor: Ajit Srivastava, Ph.D.

An abstract of
A dissertation submitted to the Faculty of the
James T. Laney School of Graduate Studies of Emory University
in partial fulfillment of the requirements for the degree of
Doctor of Philosophy
in Physics
2019

Abstract

Single Photons, Phonons and Valley-Locked Spins in Atomically Thin WSe₂

By Xiaotong Chen

Single-photon emitters or optically active quantum dots (QDs) in atomically thin WSe₂, comprised of localized bound electron-hole pair, exhibit a variety of optical properties, such as the single-photon emission and the spin-valley degree of freedom which may find potential application in quantum information processing, quantum sensing and exploring fundamental many-body quantum physics. In this dissertation, we explore the interaction between single QDs and phonons or charge carriers in the monolayer WSe₂ at low temperature down to 4 K and high magnetic up to 8 T. Experimentally, we observed an entanglement state between phonons carrying pseudo angular momentum (chiral phonons) and single photons arising due to unique electronic and phononic properties. We also investigated an optical initialization of a single spin-valley state which can be exploited in quantum information processing. In addition, by studying the phonon sideband, the intrinsic properties of QDs, such as the size and interaction type with phonons are revealed.

The first part demonstrates the entanglement between the single photons and chiral phonons. The doubly degenerate chiral phonons interacting with the neutral QDs lead to phonon replica peaks at lower energy. The phonon replica and its parent neutral QD originate from the same QD as they exhibit an identical spectral jittering pattern. However, the emission from neutral QD is linear polarized whereas the phonon replica exhibits an unexpected random

polarization at zero magnetic fields. As the phonon replica results from a coherent phonon scattering process, the unpolarization at zero magnetic fields is intriguing. This behavior arises due to the entanglement state formed by two indistinguishable scattering paths of the single photons and chiral phonons. Under the perpendicular magnetic field, because the indistinguishability is lost and the entanglement state is destroyed, the phonon replica and parent neutral QD both recover the circular polarization.

In the second part, we studied the optical initialization of a single spin-valley state in the single positively-charged QD. The singlet QD has a similar spectral jittering as a neutral QD indicating the same origination and exhibits spectral features consistent with a single positively-charged QD. Under a perpendicular magnetic field, the emission polarization of the charged QD can be selectively controlled by choosing the helicity of the excitation laser but this phenomenon is absent in neutral QDs. In other words, the spin-valley state of the excess hole is optically initialized by the helicity of the excitation laser as its spin-valley state is opposite to the recombined electron-hole pair in the single positively-charged QD. We explain the spin-valley initialization as a result of the quenching of exchange interaction in single positively-charged QDs.

Finally, after calculating and fitting the phonon sideband, we estimate the intrinsic properties of QDs, such as the size and coupling type with phonons in monolayer WSe₂. The spectral calculation of QDs is conducted within the independent boson model and under different coupling types between QDs and phonon modes. Our spectral calculations exhibit a good fitting to the experimental results, especially for the phonon sideband at the low energy side. The size of QDs is estimated at about 4 nm and the coupling type is the deformation coupling between QDs and acoustic phonon modes. The fidelity

of the fitting is about 60% to 70% at different temperatures and it can be enhanced by improving the fitting effect of phonon sideband at high energy side.

Single Photons, Phonons and Valley-Locked Spins in Atomically
Thin WSe₂

by

Xiaotong Chen

B.S., Shandong University, P.R. China, 2015

Advisor: Ajit Srivastava, Ph.D.

A dissertation submitted to the Faculty of the
James T. Laney School of Graduate Studies of Emory University
in partial fulfillment of the requirements for the degree of
Doctor of Philosophy
in Physics
2019

Acknowledgements

I appreciate all the help from my advisor, committee members, labmates, friends and my family during my more than four years of studies at Emory University,

First and foremost, I would like to express my deepest gratitude to my advisor Prof. Ajit Srivastava. Back to the days when I joined the lab, Ajit was really nice and patient to teach me the optical experiments from a very basic level and gradually solid my background for the research topic. It was so helpful for me to efficiently start my Ph.D. journey. I feel fortunate to be shaped by Ajit in both experimental and theoretical aspects. Privately, we regard Ajit as a textbook because we can obtain a lot of new knowledge every time asking him questions. In addition, I am trained to think questions in a physicist's way which is to focus on physics rather than only mathematics. Ajit's attitude towards scientific research influenced and gradually changed me. It is more important and meaningful to enhance my physics knowledge, learn new experimental techniques and cultivate physics intuitions. It is my good fortune to obtain scientific training from Ajit. He is a great example for me to learn from and respect.

I thank my committee members, Prof. Hayk Harutyunyan, Prof. Sergei Urazhdin, Prof. Tim Lian, Prof. Justin Burton, and Prof. Sidong Lei. I appreciate the knowledge I learned in their classes and help from their group members. I also thank my labmates and our collaborators. Dr. Xin Lu and Dr. Sudipta Dubey taught me how to exfoliate and transfer monolayer samples. I thank all our collaborators, Sheng Liu, Xingzhi Wang, Prof. Qihua Xiong

at Nanyang Technological University, Prof. Lifa Zhang at Nanjing Normal University and Prof. Atac Imamoglu at ETH Zurich. I thank the generous help regarding SEM, thermal evaporation and other equipments from Dr. Andrei Zholud, Dr. Ryan Freeman, Guanxiong Chen, Robert Lemasters, and Chentao Li. And it is inspiring to talk with our group members Qiang Yao and Weijie Li.

I am very fortunate to meet many friends at Emory. They give me a lot of valuable advice and information for both academic research and daily life. I really appreciate the generous help they gave me when I am having a hard time.

I thank my mathematics teacher Mr. Xueqian Wu at primary school. He gave me the initial confidence to believe my potential and it will influence my whole life. No matter what difficulty emerges, I have the courage to challenge it.

In the end, I thank my parents and sister for their unconditional support and trust. Especially when the accident happened to our family, my sister behaved stronger than me to take the responsibility.

To my family

Contents

1	Introduction	1
1.1	Transition metal dichalcogenides (TMDC)	1
1.2	Exciton and quantum dot in monolayer WSe ₂	3
1.3	Exciton valley depolarization	6
1.4	Chiral phonons in monolayer hexagonal lattice	9
2	Experimental Methods	14
2.1	Device fabrication	14
2.2	Magneto-optical PL measurement	17
3	Entanglement between single photon and chiral phonon in monolayer WSe₂	21
3.1	Sample review	21
3.2	Phonon replica of neutral quantum dot	23
3.3	Power dependence and Zeeman splitting	28
3.4	Polarization measurements	32
3.5	Single photon and chiral phonon entanglement	35
3.6	Polarization recovery under magnetic field	38
3.7	PLE & localization of QDs & Raman symmetry analysis	41
3.7.1	PLE	41

3.7.2	Localization of QDs	41
3.7.3	Raman symmetry analysis	42
3.8	Conclusion and Perspectives	44
4	Optical initialization of quantum dot with a single spin-valley	45
4.1	Single spin-valley control mechanism	45
4.2	Positively charged quantum dot	48
4.3	Polarization resolved magneto-optical measurement	53
4.4	Single spin-valley initialization	56
4.5	Conclusion and Perspectives	60
5	Phonon sideband in QD spectra	61
5.1	Electron-phonon interaction	61
5.2	Estimation of the size of QDs	63
5.3	Conclusion and Perspectives	69

List of Figures

1.1	The figure shows the top view of TMD monolayer, the blue and orange spheres represent M and X atom respectively. The enlarged side view is a prismatic structure marked in a triangle in the right figure. The bottom left figure represents the hexagonal Brillouin zone. Figure adopted from Ref. [11].	3
1.2	Schematic representation of the spin-valley locking in monolayer WSe ₂	4
1.3	Photoluminescence of exciton, trion and broad defect peaks measured in monolayer WSe ₂ with HeNe laser at 4.2K temperature. Figure adopted from Ref. [29].	5
1.4	Sharp PL spectra of QD with a linewidth as narrow as 45 ueV in monolayer WSe ₂ measured at 4 K. γ is the full width at half maximum	6
1.5	The second-order photon correlation function $g^{(2)}(t)$ of PL measured with a HBT setup. An antibunching dip proves QD in monolayer WSe ₂ as a single photon emitter. Figure adopted from Ref. [29].	6
1.6	The exchange interaction of the neutral exciton in monolayer WSe ₂ . Figure adopted from Ref. [34].	7

1.7	The four configurations of the negative trion in monolayer WSe ₂ . Figure adopted from Ref. [34]	8
1.8	The exchange interaction of the positive trion in monolayer WSe ₂	9
1.9	a) Phonon dispersion of a honeycomb AB lattice. b) Non-local part phase correlation for sub-lattice A and B. c) The PAM for bands from 1 to 4 at valley \mathbf{K} and $-\mathbf{K}$. This phonon disper- sion is calculated with longitudinal (transverse) spring constant $K_L=1$ ($K_T = 0.25$) and $m_A=1$ and $m_B=1.2$. Figure adopted from Ref. [47]	12
1.10	A: Creation mechanism of chiral phonon and B: PL's polariza- tion of B exciton. Figure adapted from Ref. [49]	13
2.1	Picture of the sample transfer setup.	15
2.2	The optical image of the monolayer WSe ₂ /BN stack under the white light illumination. The blue part represents hBN and the red part is monolayer WSe ₂	16
2.3	Cartoon image of the monolayer WSe ₂ sample and source-drain current measurement at a different back-gate voltage.	16
2.4	Schematic representation of the home-built confocal magneto- optical setup used to measure the quantum dots in monolayer WSe ₂	17

2.5	Schematic of the setup for polarization measurements avoiding the influence of QDs' blinking. The Wollaston prism separates the s and p components. A half wave-plate is used for linear basis measurement and a quarter wave-plate is used for circular basis measurement to convert circularly polarized components into linear polarized components. The quarter wave-plate converts s and p component into circularly polarized light so the signal is insensitive to the grating efficiency.	19
2.6	Polarization of phonon replica measured in a linear basis and circular basis. The dashed line in the left (right) figure shows the ideal linear (circular) polarization behavior. The solid line in the left (right) figure shows the ideal circular polarization or unpolarization (linear polarization or unpolarization).	20
3.1	PL of monolayer WSe ₂ measured at room temperature. A prominent asymmetry peak centered at 1654 meV (750 nm) arises proving the sample is monolayer. The excitation laser is HeNe laser with the power of 16 μ W.	22
3.2	PL of the monolayer WSe ₂ measured at room temperature. A prominent asymmetry peak centered at 1654 meV (750 nm) arises proving the sample is monolayer. The excitation laser is a HeNe laser with a power of 16 μ W.	22
3.3	PL intensity map as a function of back-gate voltage. The attractive Fermi-polaron (X_{ap}) and free exciton (X^0) are identified. The QDs arise at a similar gate voltage of the broad defect peak which indicates the QDs originates from monolayer WSe ₂	23

3.4	Gate-voltage dependent PL of QDs. The triangles and squares (stars) mark the spectral jittering between D3a and D3b (D4a and D4b). The dashed lines show the gate voltage where different QDs arise simultaneously.	25
3.5	The cross-sectional PL spectrum at the gate voltage of -78 V. The splitting energies in doublet a and doublet b have the same value and the energy difference between a and b doublets is 21.8 meV for all the groups. The inset shows the PL of another doublet group at a gate voltage of -70 V.	25
3.6	Three other doublet groups. The energy difference between doublet a and doublet b is also 21.8 meV.	26
3.7	Phonon dispersion of monolayer WSe ₂ . At Γ -point, two optical phonon modes, LO(E'') and TO(E'') are degenerate in energy. Their oscillation modes can be combined to form two new modes. The two new modes have pseudo angular momentum (PAM) of 1 or -1.	27
3.8	Raman scattering results in WSe ₂ samples with different layers. For the WSe ₂ samples with more than 2 layers, a Raman peak at 176 cm ⁻¹ corresponding to an energy of 21.8 meV is observed.	28
3.9	Power dependence of D3a and D3b doublet. The x-axis and y-axis are plotted in a log scale. In D3 group, the four peaks in D3a and D3b exhibit similar power dependence with a ratio of about 0.86.	29
3.10	Power dependence of D2 group. In D2 group, D2a and D2b exhibit similar power dependence with a ratio of about 0.6.	30

3.11	The g-factor for D3a and D3b. This figure shows the splitting energy of D3a and D3b doublets in the magnetic field. By fitting the energy difference, the g-factors are calculated with the value of $8.9 \mu_B$ and $9.3 \mu_B$	30
3.12	The polarization measurement results of D3a doublet in a linear basis. In a linear basis, the dashed red and blue lines represent the two orthogonal ideal linearly polarized light. The red (blue) solid dots correspond to the experimental polarization of D3a red (blue) peak.	33
3.13	Unpolarization of the D3b red peak. The left (right) picture represents the result in a linear (circular) basis. In the linear basis, the orange dashed line represents the ideally linear polarization and the solid red line represents the ideally circular or random polarization. In the circular basis, the green dashed line represents the ideally circular polarization and the solid line corresponds to the ideally linear or random polarization. The blue dots are the experimental results for polarization measurement. Based on these measurements, the D3b red is concluded with completely random polarization.	33
3.14	Polarization measured in both linear and circular basis. D4a doublet is orthogonal linearly polarized and D4b red peak is unpolarized.	35
3.15	Real and imaginary parts of the density matrix of D4b red peak. The diagonal value of 0.5 in the matrix of real parts shown in the left picture corresponds to a completely mixed state.	35

3.16	Schematic of entanglement between single photons and chiral phonons. The chiral phonons with PAM of +1 and -1 are degenerate and the left and right circularly polarized lights are also degenerate due to the time-reversal symmetry. From the selection rules of the chiral phonon, the left (right) circularly polarized photon can only couple to chiral phonon with PAM of +1 (-1) to produce a scattered photon with the right (left) circularly polarization. As the two scattering process are indistinguishable, the scattering process can be present as an entanglement state. .	37
3.17	The polarization of D2a and D2b in an out-of-plane magnetic field. The D2a and D2b peaks recover right (left) circular polarization under positive (negative) magnetic field.	39
3.18	Circular dichroism under different magnetic fields for D3a blue and D3b blue peaks.	39
3.19	Helicity-resolved Raman scattering measurement of E'' ($E_g/E'/E_{1g}$) mode under non-resonant excitation. The polarization of the incident laser is σ^+ . E_g/E' mode exhibit σ^- polarization from 2-5L WSe ₂ and only with a small component of σ^+ . For 6L, 7L and bulk (15nm), the opposite polarization effect becomes weaker. The excitation laser has a wavelength of 446.1 nm and 0.5 mW.	40

3.20	<p>PLE of D2a D3a and D4a doublet. The black dashed line marks the emission energy of the doublet and the orange dash-dot line indicates the free exciton's energy. As the excitation energy increases, the defect states exhibits a broad background in the spectra which is marked as the brown shaded regions. The extracted PLE in the shaded region can not fully reflect the PLE. However, the prominent peak with 53 meV higher energy than the doublet peak indicates the 2s state of the QD.</p>	42
3.21	<p>Spatial localization of the QDs in the monolayer WSe₂ FET device. Figure a shows the sample under an optical microscope. The dashed square marked in figure a indicates the scanning region whose size is about $1 \times 16 \mu m^2$. b-e shows the PL intensity map of D2a red peak (1662.4meV), D3a red peak (1638.2meV), D4a red peak (1640.2meV) and D6a red peak (1599.3meV). During the spatial scan, the gate voltage is -80V and the excitation wavelength is 732.5nm with the power of 300nW.</p>	43

4.1	Schematic illustration of single-particle states comprising two (one) electron and one (two) holes. The top part represents the two bright configurations of the negatively charged trion that one electron and one hole are located in the same valley with the same spin and the other electron are located in the same valley or opposite valley. The long-range exchange interaction between the electron and hole in the same valley with the same spin mixes the two configurations. But for the single positively charged trion shown in the bottom part, the long-range exchange interaction is strongly suppressed by Pauli blocking as the long-range exchange interaction leads to two holes located at the same valley with the same spin. The blue (red) line means the electron band with spin up (down).	47
4.2	Schematic of monolayer WSe ₂ field-effect transistor device. The monolayer WSe ₂ sample is above a few-layered BN. Changing V_g can control the doping level in the monolayer.	48
4.3	The FET current I_{sd} at different gate voltages measured with a source-drain voltage of 2V. The arrows indicate forward or backward sweeps.	48
4.4	PL intensity at different gate voltages and the cross-sectional PL spectra at a specific gate voltage in the PL maps on the left. D1/S1 or D2/S2 appear at the same gate voltage and have the same spectral jittering. The energy difference between singlet and doublet in each group is around 10 meV.	49

4.5	PL intensity at different gate voltage and the cross-sectional PL spectra at a specific gate voltage in PL maps on the left. D6 and S6 appear at same gate voltage and have the same spectral jittering. The energy difference between singlet and doublet in each group is around 10 meV.	50
4.6	Power dependence of S1/D1 group. The intensity and power axes are plotted on a log scale. The lines fit the sublinear power-law that I is proportional to P^α	51
4.7	Power dependence of S2/D2 group. The intensity and power axes are plotted on a log scale. The lines fit the power law, I proportional to P^α	51
4.8	Intensity correlation between D1 and S1. Marked by the orange (grey) arrow, when D1 intensity becomes stronger (lower) the S1 intensity becomes weaker (stronger).	52
4.9	The extracted relative intensity of S1 (blue dots) and D1 (red dots). The wavelengths of the excitation laser for S1/D1 and S2/D2 are 735 nm and 747 nm.	52
4.10	PL maps of S1/D1 and S2/D2 groups under different magnetic fields.	53
4.11	The splitting energy of S1, D1, S2, and D2. By fitting the splitting energy difference, the g-factors for singlet are around 13 and for doublet is around 10. The energy difference of the doublet under zero magnetic field is about 0.5 meV consistent with previous studies.	54

4.12	Color plot of DCP $(I_{\sigma^+}-I_{\sigma^-})/(I_{\sigma^+}+I_{\sigma^-})$ under the linear excitation. At zero magnetic field, the singlet does not have a circular component but the DCP increases when the magnetic field is increasing.	55
4.13	DCP of the two split peaks of S1. At even a low magnetic field about 0.5 T or -0.5 T, the two peaks recover sizeable circular components.	55
4.14	Polarization of S1 and S2 measured in a linear basis. The intensities of S1 and S2 do not change when the polarizer is rotated. Combining the 0 DCP value measured at zero magnetic field, the singlet is unpolarized.	56
4.15	The PL intensity maps of S2 under a perpendicular magnetic field. With σ^+ , σ^- or a linearly polarized light as excitation, the PL of S2 exhibits different peaks. Under σ^+ (σ^-) excitation, only σ^+ (σ^-) emission is observed. Under the linear polarized excitation, both peaks are observed.	57
4.16	Extracted B dependent ratios, $(I_{B^+} - I_{B^-})/(I_{B^+} + I_{B^-})$ of the S2 red peak, where I_{B^+} (or I_{B^-}) denotes the positive (or negative) magnetic field. At the high magnetic field, the ratio approaches to nearly 1 implying almost completely optical initialization of the spin-valley state.	58
4.17	PL plot of S2 peak under different magnetic field with σ^+ , σ^- or π (linear) excitation.	58
4.18	The extracted B dependent ratios, $(I_{B^+} - I_{B^-})/(I_{B^+} + I_{B^-})$ of the S2 red peak.	58

4.19	PL color plot of D2 doublet with detuning energy similar to laser energy for exciting S2 peak.	59
4.20	B-dependent ratio $(I_{B^+}^N - I_{B^-}^N)/(I_{B^+}^N + I_{B^-}^N)$ where $I_{B^+}^N$ ($I_{B^-}^N$) denotes the red peak intensity normalized by the intensity sum of the blue and red peaks. Almost no difference between σ^+ or σ^- excitation is observed.	59
5.1	Spectral fitting with a size parameter from 3 nm to 20 nm for the red peak of the dot with a phonon sideband. The blue dots are the spectra of the quantum dot. The solid lines are the calculated spectra.	66
5.2	Spectral fitting for the doublet quantum dot at different temperatures. The dots are experimental results and the solid lines are the calculated spectra.	67
5.3	Fitting fidelity. The fidelity is about 60-70%.	68

List of Tables

3.1	g-factor of doublet a and b in D1, D2, D3 and D5.	31
3.2	Huang-Rhys factor for all the groups	31
4.1	g-factors for the singlets and doublets in three groups.	53

Chapter 1

Introduction

1.1 Transition metal dichalcogenides (TMDC)

Graphene is an atomically thin carbon layer with a honeycomb structure and a corresponding hexagonal Bravais lattice. Since its first isolation in 2004 [1,2], graphene has been found to have extraordinary mechanical and electronic quality. Its discovery heralded the emergence of atomically thin 2D materials - a new material platform with rich and new physics. Specifically, one family of 2D materials, atomically thin transition metal dichalcogenides (TMDs) has attracted significant attention because of their unique optical and electrical properties.

2D atomically thin TMDs materials have a form of MX_2 with M a transition metal atom (W or Mo) and X a chalcogen atom (S, Se or Te). Their crystal structure is similar to graphene's hexagonal lattice but the neighboring atoms are different as an M atom on one site enclosed by two X atoms on the other site as shown in figure 1.1 [3, 4]. Due to this difference, the inversion symmetry in TMDs is broken which leads to a band gap at the K-point of the Brillouin zone.

Unlike bulk TMDs having an indirect bandgap in the center of the Brillouin zone, the monolayer TMDs exhibit a direct bandgap at K-point which lies in the visible and near-infrared light range and therefore can have applications in electrical transistors, LED emitters and photo detectors. The inversion symmetry breaking also leads to a valley-contrasting Berry phase and magnetic moments in K and -K valleys. By adding an in-plane electric field, the valley Hall effect induced by the valley-contrasting Berry phase has been observed in both graphene [5–7] and TMD systems [8, 9].

Furthermore, TMD materials have a strong spin-orbit coupling at the scale of 100 meV. For example, in monolayer WSe₂, the spin-splitting in valence band at K-point is 450 meV and in conduction band is 40 meV [10–12]. For the interband transition of the electron between the valence band and the conduction band, the coupling strength with the helicity of optical fields (σ^\pm -polarization) is [14]

$$|P_\pm(\mathbf{k})|^2 = \frac{m_0^2 a^2 t^2}{\hbar^2} \left(1 \pm \tau \frac{\Delta'}{\sqrt{\Delta'^2 + 4a^2 t^2 k^2}}\right)^2 \quad (1.1)$$

where a is the lattice constant, t is the effective hopping integral, τ is 1 (-1) in K (-K) valley, \mathbf{k} is the wavevector difference away from the K or -K-point and Δ' is the spin-dependent bandgap which is much larger than atk . Therefore at K-point (-K-point), P_- (P_+) = 0 which produces the valley-dependent optical selection rules. The inversion symmetry breaking together with the spin-orbit splitting leads to a spin-valley locking in K and -K-point [13, 14]. The optical selection rules indicate that a photon with σ^+ (σ^-) polarization can only couple to K (-K) valley shown in figure 1.2.

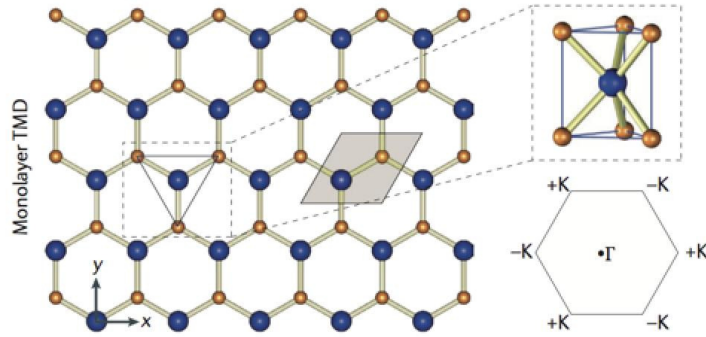


Figure 1.1: The figure shows the top view of TMD monolayer, the blue and orange spheres represent M and X atom respectively. The enlarged side view is a prismatic structure marked in a triangle in the right figure. The bottom left figure represents the hexagonal Brillouin zone. Figure adopted from Ref. [11].

1.2 Exciton and quantum dot in monolayer WSe_2

In semiconductors, upon absorbing a photon, the electron from the valence band is excited into the conduction band leaving a vacancy in the valence band which can be considered as a “hole” with a positive charge. The excited electron is bound with the positive charge hole by Coulomb interaction and the electron-hole pair forms a hydrogen-like state, called the exciton. Due to the reduced screening effect owing to the atomically thin geometry [15–17], excitons in TMD materials have a large binding energy around 0.3-1 eV [18–20] which is about one order of magnitude larger than the binding energy of excitons in bulk TMDs [21] and GaAs [22]. The exciton can capture an excess electron or hole to form a charged state called trion and compared to an exciton, trion has an additional binding energy about 18-40 meV. The exciton’s Bohr radius is on the order of 1 nm indicating that the excitonic wavefunction expands over several unit cells [23–27]. Therefore, the exciton in TMDs can be considered as Wannier type exciton localized in momentum space around K-point. As shown in figure 1.2 which shows the band structure around K-point in monolayer

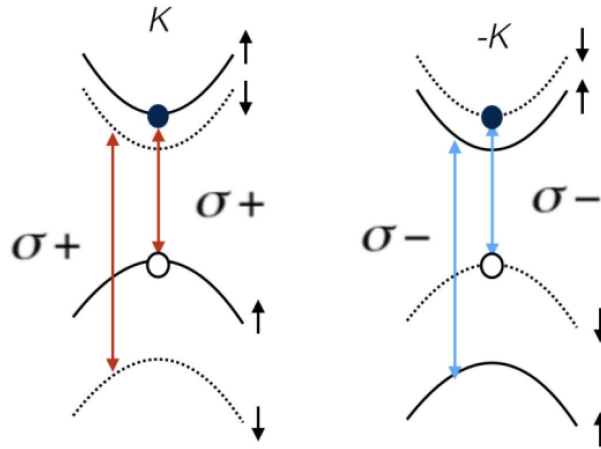


Figure 1.2: Schematic representation of the spin-valley locking in monolayer WSe_2 .

WSe_2 , the exciton comprised of electron and hole with the same (opposite) spin is called the bright (dark) exciton. Excitation light with an in-plane (out-of-plane) electromagnetic field can interact with the bright (dark) exciton. For the bright exciton configurations in one valley, the low energy bright exciton is usually called A exciton and high energy one is called B exciton. Figure 1.3 shows the exciton and trion photoluminescence spectra in monolayer WSe_2 . In the photoluminescence, a broad peak shows at the 20-100 meV lower energy side compared to the exciton and trion peak and it is attributed to the defects or impurities in WSe_2 [28]. Exciton and trion peaks exhibit a linear power dependence but the broad defect peak shows a saturation behavior at high excitation power as the energy band of the defects or impurities is not continuous.

The broad peak region of monolayer WSe_2 exhibits significant sharp lines which can be as narrow as $45 \mu\text{eV}$ limited by our instrument resolution shown in figure 1.4. These sharp lines are originating from the excitons trapped by localized minimum potentials and called single-photon emitters or quantum dots

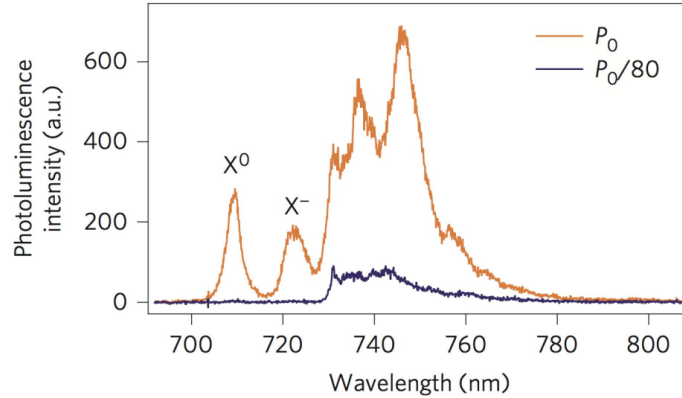


Figure 1.3: Photoluminescence of exciton, trion and broad defect peaks measured in monolayer WSe₂ with HeNe laser at 4.2K temperature. Figure adopted from Ref. [29].

(QDs). The positions of the localized QDs are usually randomly distributed in the regions of defects or impurities in monolayer WSe₂. It is reported that by adding strains in the sample, the positions of QDs can be deterministically controlled [30].

QDs have a longer lifetime at the level of nanosecond [29, 31, 32] which is much longer than that of the free exciton, about picoseconds at low temperatures. The QDs in monolayer WSe₂ are single-photon emitters as an “antibunching” dip is observed in the photon correlation measurements with $g^{(2)}(0) < 0.5$ shown in figure 1.5. The second correlation function $g^{(2)}(0) = \frac{\langle \hat{n}(\hat{n}-1) \rangle}{\langle \hat{n} \rangle^2}$ where \hat{n} is the photon number observed in the Hanbury-Brown-Twiss (HBT) setup at the same time. If it is smaller than 0.5, the photon source must be a single-photon emitter. The QDs in TMDs can inherit the electronic properties from the host material such as the valley degree freedom. Under a high magnetic field in a Faraday configuration, both neutral and charged QDs splits into two peaks with circular polarizations. We will demonstrate the detailed polarization properties of QDs in the main chapters. In the next chapters, we

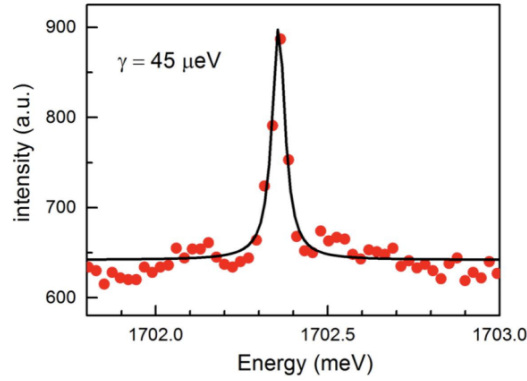


Figure 1.4: Sharp PL spectra of QD with a linewidth as narrow as 45 ueV in monolayer WSe₂ measured at 4 K. γ is the full width at half maximum

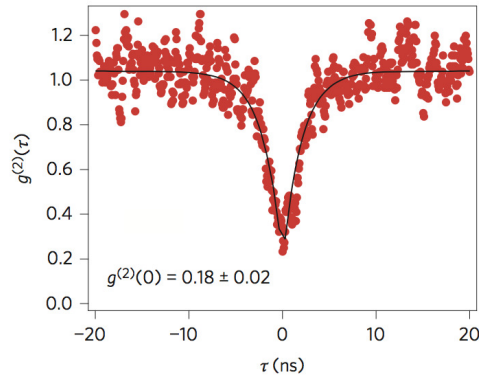


Figure 1.5: The second-order photon correlation function $g^{(2)}(t)$ of PL measured with a HBT setup. An antibunching dip proves QD in monolayer WSe₂ as a single photon emitter. Figure adopted from Ref. [29].

show the new physical properties of QDs in a field-effect transistor device of monolayer WSe₂ which allows us to controllably switch on and off the emission of QDs together with introducing extra electrons or holes in the sample.

1.3 Exciton valley depolarization

The optical initialization and manipulation of a single spin and its intrinsic freedoms are vital in the spin-photon interface, quantum communication, quantum information, and quantum sensing. The application of the valleytronics

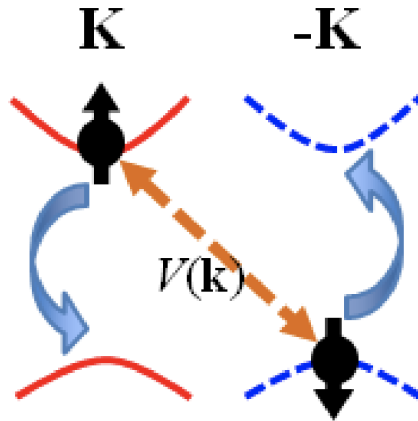


Figure 1.6: The exchange interaction of the neutral exciton in monolayer WSe₂. Figure adopted from Ref. [34].

requires a longer valley polarization lifetime. For the free electrons and holes, the intervalley scattering needs large momentum transfer due to the large momentum difference between K and -K valley. The spin-valley locking requires a spin-flip for the valley depolarization and in absence of magnetic impurity, the valley lifetime of the free electrons and holes is enhanced. The hole's valley lifetime is measured to be 1 ns (around 200 ps) at low (room) temperature [33].

For the free bright excitons in monolayer WSe₂, compared to the free charge carriers, another important valley depolarization process called the exchange interaction should be emphasized. The exchange interaction in the free exciton results from the indistinguishability of particle and leads to a virtual annihilation and creation of the hole in the valence band and the electron in the conduction band. As shown in figure 1.6 the virtual annihilation of the hole and electron in K valley results in an appearance of the electron-hole pair at -K valley and thus mix the two valley states. The whole process does not involve an intervalley scattering and spin-flip process. The exchange interaction coupling between the neutral exciton states in K and -K valley can be written as [34–36]

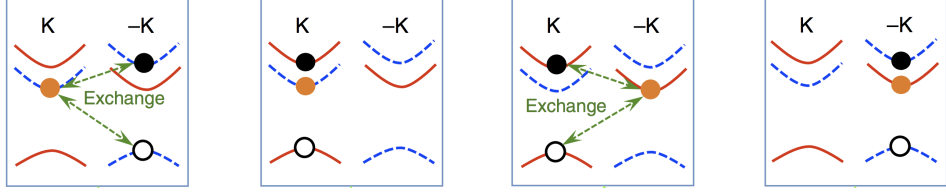


Figure 1.7: The four configurations of the negative trion in monolayer WSe₂. Figure adopted from Ref. [34]

$$\hat{H} = \hbar\omega_0 + \frac{\hbar^2 k^2}{2M_0} - \frac{k}{K} J e^{-2i\theta} \hat{\sigma}_+ - \frac{k}{K} J e^{2i\theta} \hat{\sigma}_- \quad (1.2)$$

and leads to an energy splitting

$$E_{\pm}(k) = \hbar\omega_0 + \frac{\hbar^2 k^2}{2M_0} \pm J(k) \quad (1.3)$$

where k is the center-of-mass momentum of the exciton $\hbar\omega_0$ is the exciton energy at $k=0$, and M_0 is the exciton mass.

For negative trion state in monolayer WSe₂, the exchange interaction picture becomes complex. The four configurations of negative charged bright exciton states are shown in figure 1.7. The exchange interaction between the electron-hole pair in the same valley with the opposite spin can couple the two configurations with the same excess electron. The exchange interaction between the two electrons with the same spin leads to an additional energy. But for the trion states whose two electrons have different spin, the exchange interaction couples the bright trion state to dark trion state. Therefore, the exchange interaction in bright trion states can be written as

$$\hat{H}_- = \hbar\omega_- + \frac{\hbar^2 k^2}{2M_-} - \frac{k}{K} J e^{-2i\theta} \hat{\sigma}_+ - \frac{k}{K} J e^{2i\theta} \hat{\sigma}_- + \frac{\delta}{2} (\hat{\sigma}_z \hat{s}_z + 1) \quad (1.4)$$

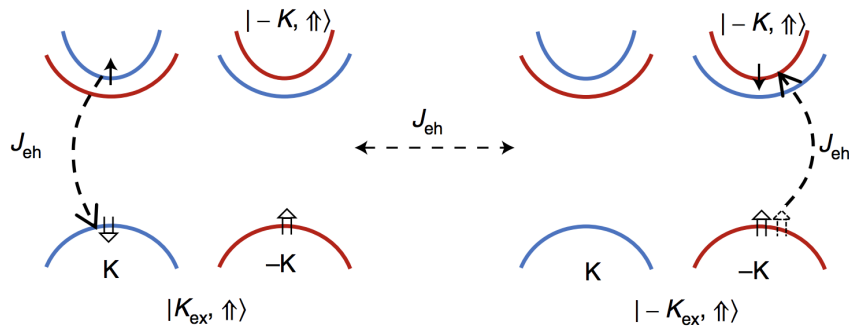


Figure 1.8: The exchange interaction of the positive trion in monolayer WSe₂

where \hat{s}_z notes the spin index of the excess electron. The exchange interaction described above leads to a finite gap opening at zero center-of-mass momentum.

For positive trion state in monolayer WSe₂, in order to minimize the energy, the two holes are located at different valleys because of the large spin-orbit splitting in the valence band. The exchange interaction between the bright electron-hole pair can not happen as it is blocked by the Pauli principle. Therefore, the single positively-charged trion states in different K valley does not split.

1.4 Chiral phonons in monolayer hexagonal lattice

The valleytronics resulting from the inversion symmetry breaking has attracted increasing attention in transition metal dichalcogenides. The chirality of electrons in the Brillouin zone corners (K-points) provides another freedom to manipulate. Recently, helicity-resolved Raman scattering observed the photon's helicity change involving the phonon at Γ -point [76]. I will follow the theoretical paper [47] by Prof. Lifa Zhang to introduce the properties of chiral phonons in monolayer TMDCs.

The monolayer TMDCs have two sub-lattices and it corresponds to two sub-lattice unit cells in the unit cell of monolayer. Similar to the polarization definition of the light, the new basis of right-handed or left-handed circular polarization for the two sub-lattices is defined as $|R_1\rangle = \frac{1}{\sqrt{2}} \begin{bmatrix} 1 & i & 0 & 0 \end{bmatrix}^T$, $|L_1\rangle = \frac{1}{\sqrt{2}} \begin{bmatrix} 1 & -i & 0 & 0 \end{bmatrix}^T$, $|R_2\rangle = \frac{1}{\sqrt{2}} \begin{bmatrix} 0 & 0 & 1 & i \end{bmatrix}^T$ and $|L_2\rangle = \frac{1}{\sqrt{2}} \begin{bmatrix} 0 & 0 & 1 & -i \end{bmatrix}^T$. The phonon eigenvector can be written as $\epsilon = \sum_{\alpha=1}^n \epsilon_{R_\alpha} |R_\alpha\rangle + \epsilon_{L_\alpha} |L_\alpha\rangle$. The operator for phonon polarization in z direction is defined as $\widehat{S}_z \equiv \sum_{\alpha=1}^n (|R_\alpha\rangle\langle R_\alpha| - |L_\alpha\rangle\langle L_\alpha|)$. For the condition of monolayer, the two-dimensional vibrations of the lattice can be presented as $u_t = (u_{t1}^x u_{t1}^y u_{t2}^x u_{t2}^y)^T$ where t means the t -th unit cell, u is the displacement in x or y direction. And the angular momentum of total atomic vibrations is $\mathbf{J}^{ph} = \sum_{t\alpha}^b m_\alpha \mathbf{u}_{t\alpha} \times \dot{\mathbf{u}}_{t\alpha}$ and the angular momentum in z direction is $J_z = \sum_t u_t^T i M' \dot{u}_t$ where $M' = \begin{bmatrix} 0 & -i \\ i & 0 \end{bmatrix} \otimes \begin{bmatrix} m_1 & 0 \\ 0 & m_2 \end{bmatrix}$. After using the second quantization, the two-dimensional vibration can be represented as

$$u_{t,\alpha}^j = \sum_k \epsilon_{\alpha,j}(\mathbf{k}) e^{i(\mathbf{R}_t \cdot \mathbf{k} - \omega t)} \sqrt{\frac{\hbar}{2\omega_k N m_\alpha}} a_{\mathbf{k}} + h.c.. \quad (1.5)$$

And the angular momentum can be represented as [48]

$$J_z = \sum_{\sigma, \mathbf{k}} j_{\mathbf{k},\sigma}^z [f(\omega_{\mathbf{k},\sigma}) + \frac{1}{2}], j_{\mathbf{k},\sigma}^z = (\epsilon_{\mathbf{k},\sigma}^+ M \epsilon_{\mathbf{k},\sigma}) \hbar \quad (1.6)$$

where $M = \begin{bmatrix} 0 & -i \\ i & 0 \end{bmatrix} \otimes I_{2 \times 2}$ and $f(\omega_{\mathbf{k},\sigma})$ is the Bose-Einstein distribution. The eigenvector $\epsilon(\mathbf{k}, \sigma)$ can be calculated as

$$D(\mathbf{k}, \sigma) \epsilon(\mathbf{k}, \sigma) = \omega_{\mathbf{k},\sigma}^2 \epsilon(\mathbf{k}, \sigma) \quad (1.7)$$

where the dynamical matrix is

$$D_{\alpha\alpha'}(\mathbf{k}) = \sum_{\mathbf{R}'_t - \mathbf{R}_t} \frac{K_{t\alpha,t'\alpha'}}{\sqrt{m_\alpha m_{\alpha'}}} e^{i(\mathbf{R}'_t - \mathbf{R}_t) \cdot \mathbf{k}}. \quad (1.8)$$

$K_{t\alpha,t'\alpha'}$ is the spring constant between the α -th atom in t -th unit cell and the α' -th atom in t' -th unit cell. In the hexagonal lattice, at high symmetry points Γ , \mathbf{K} and $-\mathbf{K}$, the three-fold rotation symmetry produces a requirement for the eigenvector of lattice vibration in a unit cell that $R[(2\pi/3), z]\mathbf{u}_\mathbf{k} = e^{(-i2\pi/3)l_{ph}^{\mathbf{k}}}\mathbf{u}_\mathbf{k}$ with $l_{ph}^{\mathbf{k}} = 0$ or ± 1 . The $l_{ph}^{\mathbf{k}}$ consists of the spin pseudo angular momentum (PAM) l^s from local (intercell) part $\epsilon_{\mathbf{k},\sigma}$ and the orbital PAM l^o from the nonlocal (intercell) part $e^{i\mathbf{R}_t \cdot \mathbf{k}}$.

The phonon structure of a honeycomb AB lattice is plotted in Fig 1.9. At K-point, the fundamental reason for the non-degeneracy of the phonon modes with different PAMs is the inversion symmetry breaking and time-reversal symmetry breaking in K or -K valley. In monolayer TMDCs, the PAM change of the electron in the transition from the conduction band to the valence band at K-point should be equal to the PAM of the photon emitted as $l_c - l_v = l_{photon} = \pm\tau$. The excited electron in the conduction band can be firstly intra-valley scattered by a Γ phonon and then recombine with a hole at the valence band to emit a photon. This process is called the first-order Raman scattering. Compared to the process that the excited electron recombines with the hole in the valence band without a phonon scattering process, a selection rule requires that the PAM difference of the emitted photons should equal the scattered phonon's as $\delta l_{photon} = l_{phonon}$. The entanglement state results from two degenerate chiral phonon scattering processes.

For the spin-orbit split valence band in monolayer TMDCs, the intervalley

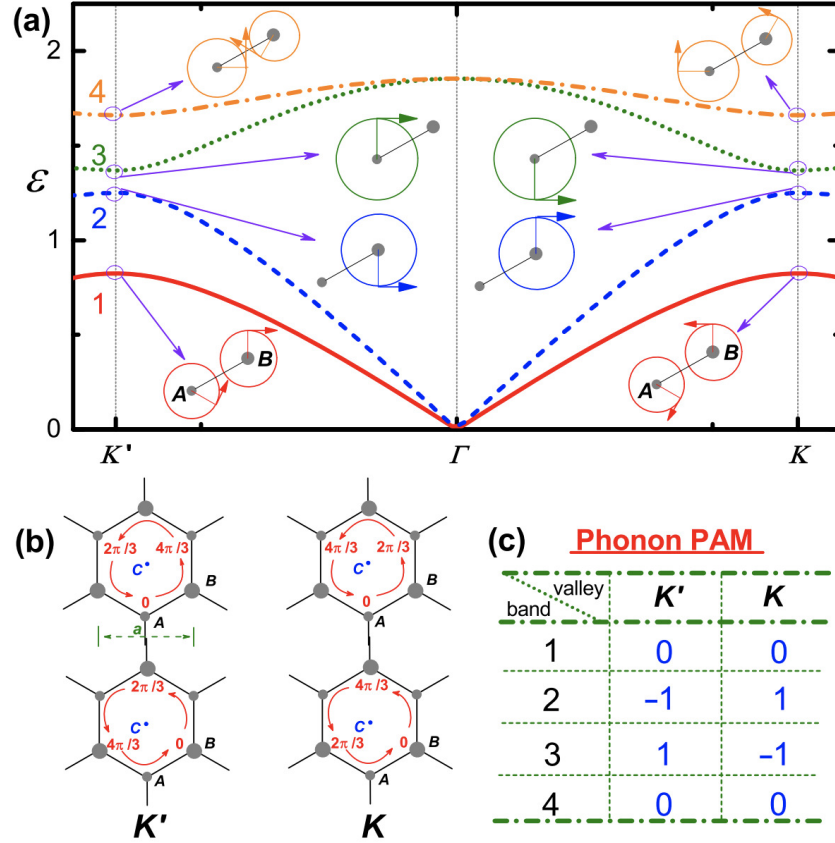


Figure 1.9: a) Phonon dispersion of a honeycomb AB lattice. b) Non-local part phase correlation for sub-lattice A and B. c) The PAM for bands from 1 to 4 at valley K and $-K$. This phonon dispersion is calculated with longitudinal (transverse) spring constant $K_L=1$ ($K_T = 0.25$) and $m_A=1$ and $m_B=1.2$. Figure adopted from Ref. [47]

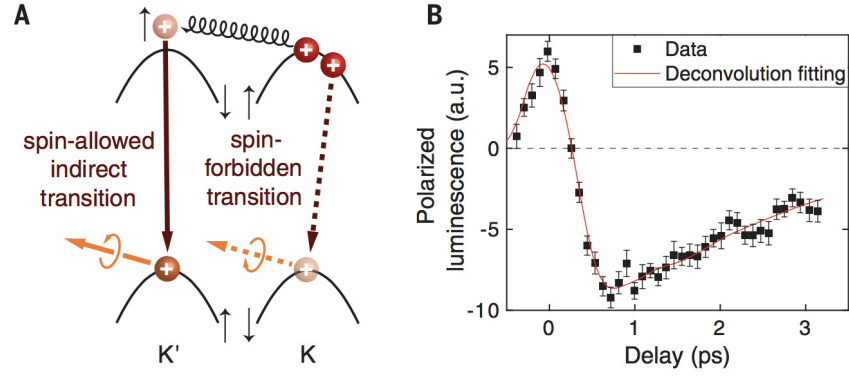


Figure 1.10: A: Creation mechanism of chiral phonon and B: PL's polarization of B exciton. Figure adapted from Ref. [49]

scattering of hole can be realized by emitting or absorbing a chiral phonon at K-point and a circularly polarized infrared photon if the energy and the angular momentum are conserved as $\Delta l_{el} = \pm l_{ph} \pm l_{photon}$ and $\lambda_{\mathbf{K}} = \pm \hbar\omega_{ph} \pm \hbar\omega_{photon}$. The chiral phonon at K-point has been observed in Ref. [49] shown in fig 1.10. The pump laser produces excited holes in K valley. Then through a virtual scattering process involving emitting a chiral phonon and absorbing an infrared photon, the hole in K valley transits into -K valley at higher energy with the same spin. Figure 1.10 B shows the polarization of B exciton. After 0.2 ps, the opposite valley polarization is observed proving the chiral phonon scattering process.

Chapter 2

Experimental Methods

2.1 Device fabrication

Since the first isolation of graphene in 2004 [1, 2], many fabrication methods have been developed to isolate 2D atomically thin TMDs such as mechanical exfoliation [39], liquid-phase exfoliation [37] and chemical vapor deposition [38]. The micromechanical exfoliation method by the scotch tape is a simple but effective way to produce high-quality samples. After attaching the surface sheets of the bulk crystal sample onto the scotch tape, the sample sheets can be transferred to another material like the polydimethylsiloxane (PDMS) or silicon substrate by slowly peeling off the scotch tape. Part of the samples transferred are randomly distributed 2D atomically thin flakes with a size of 100 to 10000 μm^2 . Under an optical microscope, monolayer TMDs can be distinguished by their characteristic colors on different substrates and confirmed by PL measurement or AFM. Finally, the monolayer sample can be positioned exactly on the target surface such as electrode made on the silicon wafer with the help of nanopositioner at a sub-micrometer resolution under an optical mi-

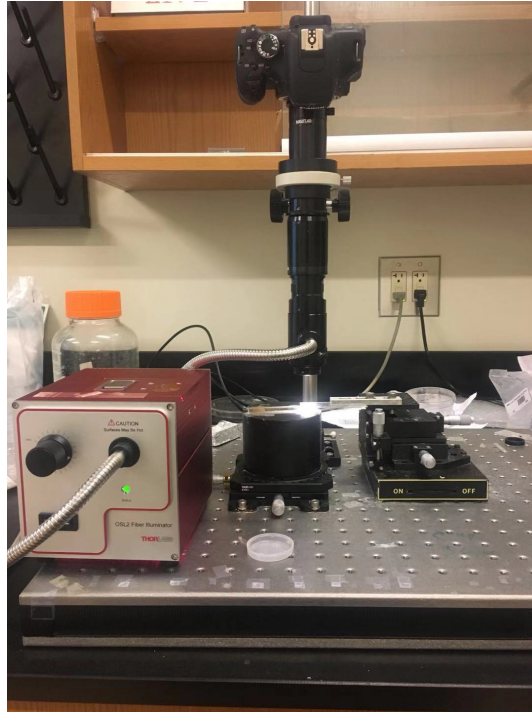


Figure 2.1: Picture of the sample transfer setup.

croscope. The van der Waals force ensures the monolayer attached to the target surface. Compared to other deterministic transfer methods like the wedging method and polyvinylalcohol method [40] which need the help of the sacrificial polymer or a wet process, the all-dry transfer method can transfer samples with no capillary force involved in the whole process and therefore has broader usability. Figure 2.1 shows our setup for transferring samples. The signal collected by the camera is inputted into television from which we can adjust the relative positions between the target sample and the transferred sample.

Using the all-dry transfer method described above, the monolayer WSe_2 we used is mechanically exfoliated on polydimethylsiloxane (PDMS) from bulk WSe_2 crystal (HQ graphene) and identified by optical contrast under the microscope. After a similar finding process, a thin hBN flake is firstly transferred onto a degenerately silicon wafer (Si^{++}) substrate with 285nm SiO_2 on the

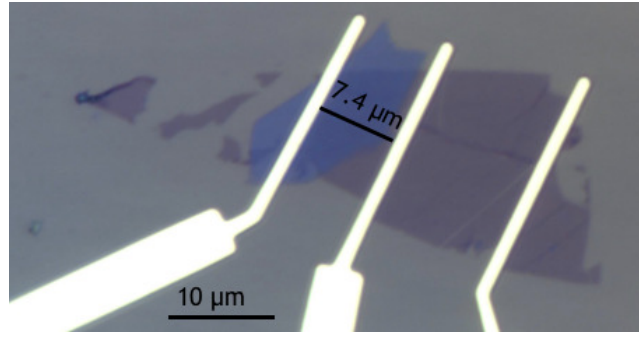


Figure 2.2: The optical image of the monolayer WSe₂/hBN stack under the white light illumination. The blue part represents hBN and the red part is monolayer WSe₂.

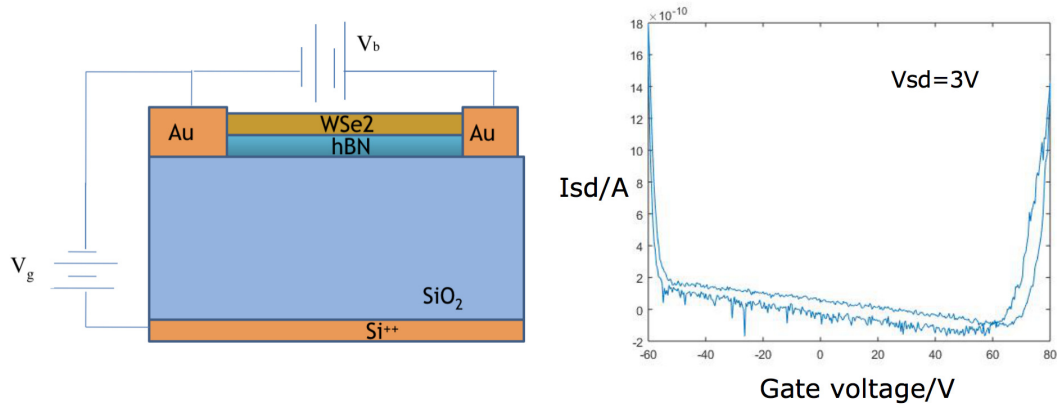


Figure 2.3: Cartoon image of the monolayer WSe₂ sample and source-drain current measurement at a different back-gate voltage.

surface. Then the monolayer WSe₂ is transferred onto hBN. The hBN underneath the monolayer WSe₂ is used to provide a flat platform and improve the sample quality. In order to control the doping level in monolayer WSe₂, 30 nm Pd/80 nm Au metal contacts are deposited on WSe₂ with electron beam lithography. Figure 2.2 shows the WSe₂ FET device where the blue part is hBN and the red part is monolayer WSe₂.

The transport property of the sample is shown in figure 2.3. A source-drain voltage 3V is applied across the sample and the current is measured at different gate voltage (different doping). This device exhibits a bi-polar effect.

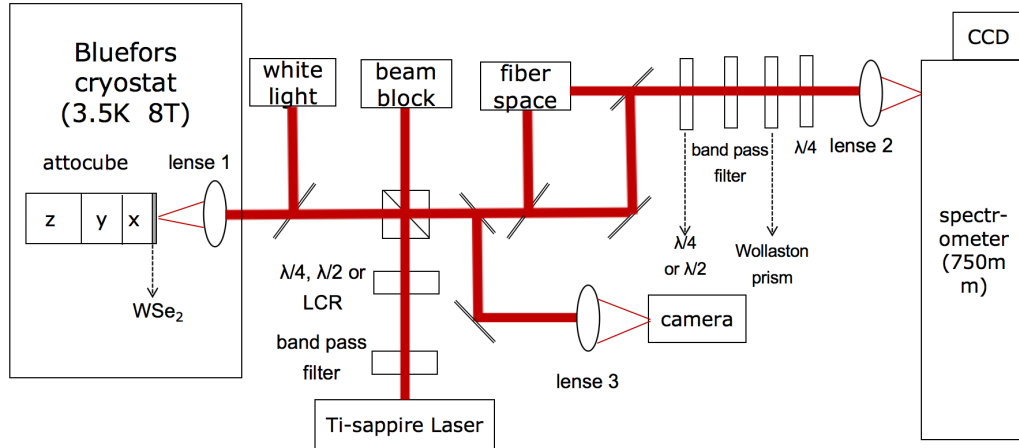


Figure 2.4: Schematic representation of the home-built confocal magneto-optical setup used to measure the quantum dots in monolayer WSe₂.

2.2 Magneto-optical PL measurement

Figure 2.4 shows the main structure of the home-built confocal magneto-optical setup used to measure the quantum dots in the monolayer WSe₂. The sample is studied at a low temperature down to 3.5 K and a high magnetic field up to 8 T in a closed-cycle cryostat (BlueFors). The cryostat is above the optical table and can be moved outside the optical table region to exchange samples. The sample position is controlled by a three-dimensional piezo scanner (Attocube Systems) with a resolution of about 200 nm controlled by ANC 300 controller. Lense 1 represents a low-temperature achromatic objective lens with an NA of 0.63 and a focal length of 3.73 mm.

In the set-up, we use white light to image the sample and usually also use a bandpass filter close to the excitation wavelength to eliminate the influence from other wavelengths. HeNe laser (632.8 nm) and a mode-hop-free tunable continuous-wave Ti-Sapphire laser (M Squared) with a resolution of 0.1 pm are used to excite the sample. A bandpass filter is put behind the laser source to narrow the excitation wavelength. And the $\lambda/4$, $\lambda/2$, liquid crystal retarder

(LCR113-B), polarizer and their combinations are put in front of the beam splitter to control the polarization of the excitation laser.

In the collection part, an aspheric lens with numerical aperture 0.55 is used to collect PL signal into a high-resolution (focal length: 750 mm) spectrometer equipped with a detector which is a liquid nitrogen-cooled charge-coupled device (Princeton Instruments SP-2750, PyLoN 1340 400 pixels CCD). In the spectrometer, the PL signal is dispersed by a grating of 1,200 grooves per mm or 300 grooves per mm (both blazed at 750 nm). A Wollaston prism separates the signal light into s and p components to avoid the influence of QDs' intensity blinking and a quarter-wave plate is placed behind it. The $\lambda/4$ waveplate can transfer the s and p components into left or right circularly polarized lights and thus eliminate the sensitivity of grating to linear polarized lights at different angles. In addition, a half-wave (super-achromatic 600-2, 700 nm, Thorlabs) or a quarter-wave (zero-order @ 780 nm) plate are placed in front of the Wollaston prism for the linear or circular measurement. The angle of the linear polarization is changed by rotating the half-wave plate. Therefore, the ratio between the intensities of the two components after the Wollaston prism behaves in different functions corresponding to different signal polarization. As the circularly polarized light becomes to linearly polarized light, by rotating the quarter-wave plate, the polarization angle of transformed linear polarized light also changes and therefore the ratio between the two components after Wollaston prism behaves in different functions corresponding to different polarizations. Besides the free space collection, the single-mode fiber is also used to collect the PL signal. A grating setup (PCG-1812-760-971) is also used to narrow the excitation or collection wavelength.

To quantify the polarization, the behavior of the ratio $I_1/(I_1+I_2)$ for differ-

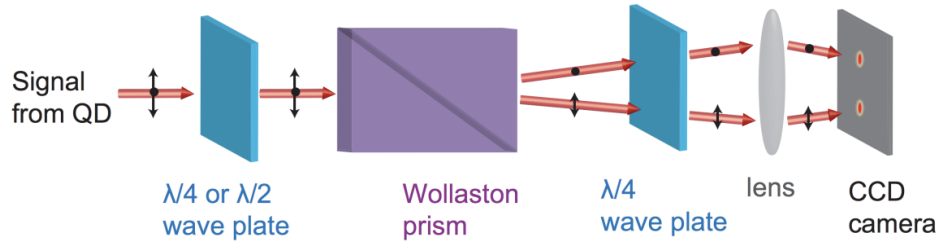


Figure 2.5: Schematic of the setup for polarization measurements avoiding the influence of QDs' blinking. The Wollaston prism separates the s and p components. A half wave-plate is used for linear basis measurement and a quarter wave-plate is used for circular basis measurement to convert circularly polarized components into linear polarized components. The quarter wave-plate converts s and p component into circularly polarized light so the signal is insensitive to the grating efficiency.

ent polarized light is plotted, for example, in fig 2.6, where I_1 and I_2 represent the intensities of the two components. In the linear basis, the orange dashed line presents a linear polarization and the red solid line represents a circular polarization or non-polarization. In the circular basis, the green dashed line represents a circular polarization and the red solid line shows a linear polarization or non-polarization.

After finding the quantum dots, the excitation wavelength of the Ti-Sapphire laser is tuned to a wavelength that the quantum dot has the maximum intensity. The magnetic field is applied perpendicular to the sample in a Faraday configuration up to 8 T.

For the Raman scattering experiment, it is conducted at room temperature with 441.6 nm He-Cd laser and 0.5 mW power. A 100× objective is used to collect the backscattered signal and direct the signal into a micro-Raman spectrometer (Horiba-HR Evo) with a grating of 1800 grooves per mm and then the signal is detected by a liquid nitrogen cooled charge-coupled device with a spectral resolution of 1 cm^{-1} .

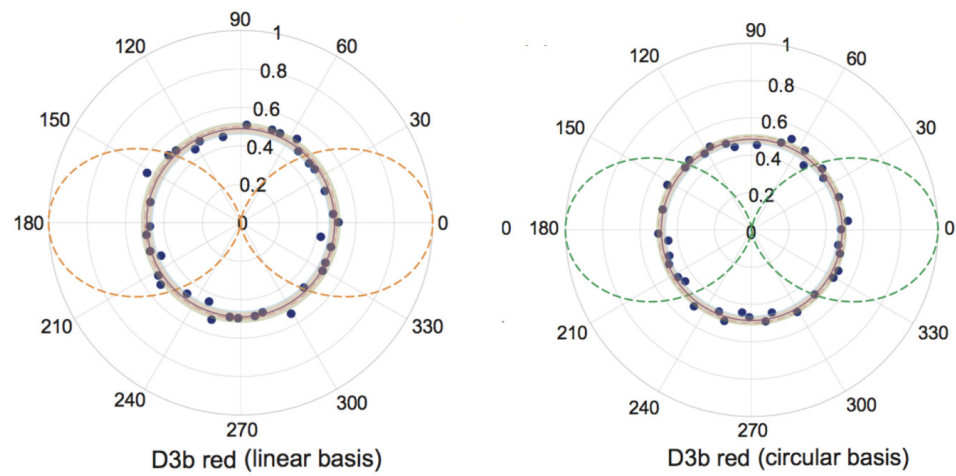


Figure 2.6: Polarization of phonon replica measured in a linear basis and circular basis. The dashed line in the left (right) figure shows the ideal linear (circular) polarization behavior. The solid line in the left (right) figure shows the ideal circular polarization or unpolarization (linear polarization or unpolarization).

Chapter 3

Entanglement between single photon and chiral phonon in monolayer WSe_2

3.1 Sample review

The sample used to measure the quantum dots is the monolayer layer WSe_2 field-effect transistor (FET) with a few layers hBN underneath to provide a flat surface. The photoluminescence (PL) of the FET sample shows a prominent and asymmetry peak centered at 1654 meV (750 nm) under HeNe (632.8 nm) excitation which verifies the monolayer properties.

Figure 3.2 shows the reflectance scan results with a white light excitation at 4 K. We can clearly see the boundary of the monolayer WSe_2 and the electrodes. At the A point marked by a red point which is on the monolayer WSe_2 with the hBN underneath, the reflection peak exhibits a clear 720 nm peak which corroborates the monolayer property.

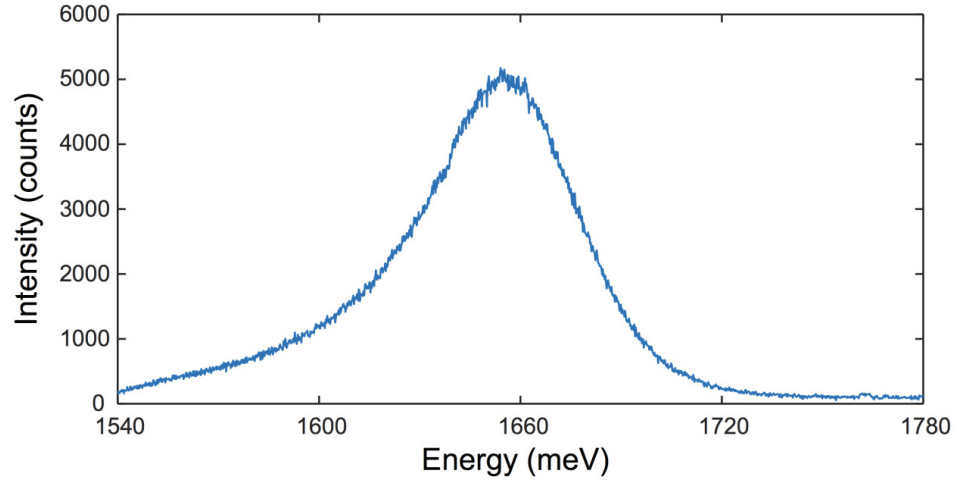


Figure 3.1: PL of monolayer WSe₂ measured at room temperature. A prominent asymmetry peak centered at 1654 meV (750 nm) arises proving the sample is monolayer. The excitation laser is HeNe laser with the power of 16 μ W.

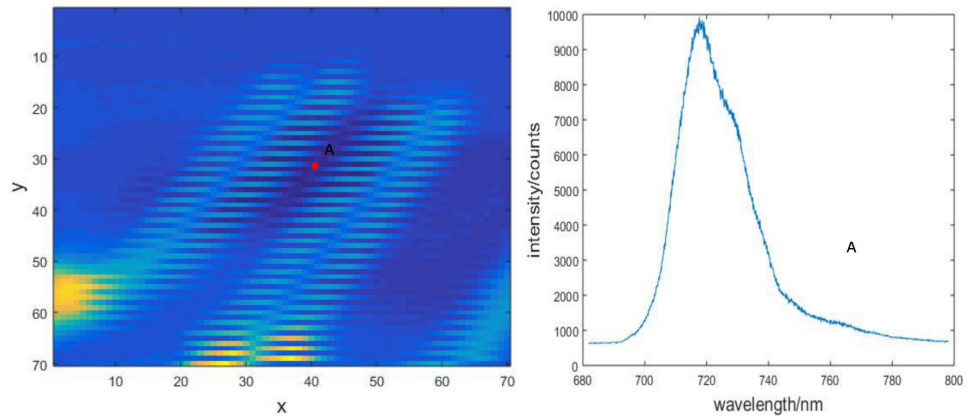


Figure 3.2: PL of the monolayer WSe₂ measured at room temperature. A prominent asymmetry peak centered at 1654 meV (750 nm) arises proving the sample is monolayer. The excitation laser is a HeNe laser with a power of 16 μ W.

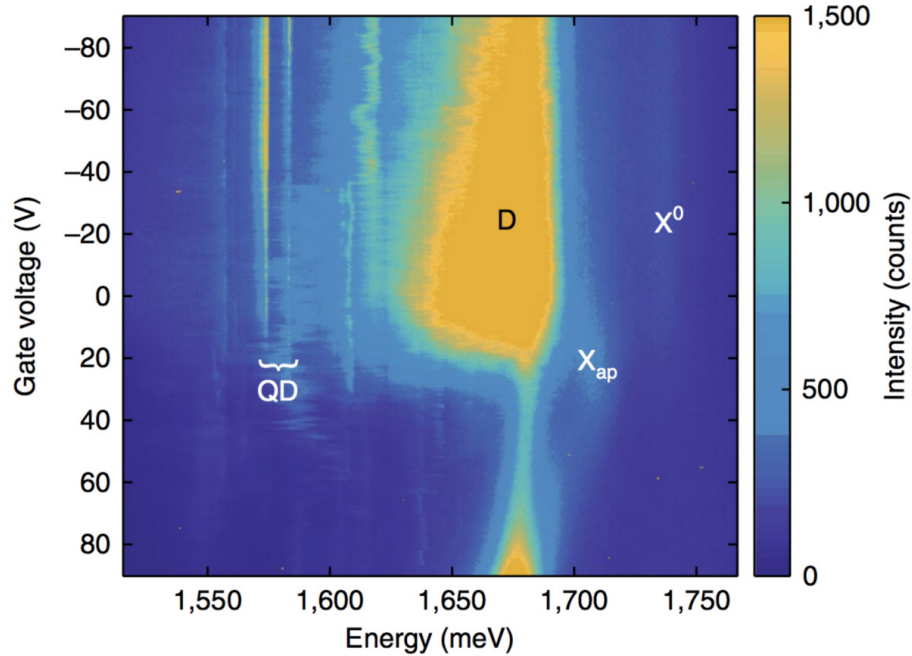


Figure 3.3: PL intensity map as a function of back-gate voltage. The attractive Fermi-polaron (X_{ap}) and free exciton (X^0) are identified. The QDs arise at a similar gate voltage of the broad defect peak which indicates the QDs originates from monolayer WSe_2 .

3.2 Phonon replica of neutral quantum dot

The photoluminescence of the monolayer WSe_2 in a field-effect transistor is measured in different doping levels controlled by changing the back-gate voltage. In figure 3.3, at +20 V gate voltage around electron doping region, an attractive Fermi-polaron peak (X_{ap}) [41] is observed. The well-known neutral exciton X^0 exhibits faint intensity at the gate range from +20 V to -90 V. The turn-on gate voltages for the broad defect peak and sharp quantum dots are both around +20 V gate voltage which demonstrates that the quantum dots are originating from the monolayer WSe_2 .

For a localized neutral quantum dot with one hole and one electron, the anisotropic electron-hole exchange interaction between the excitons at K and

-K valley is the reason for that neutral quantum dot splits into two orthogonal linearly polarized states. This fine structure splitting has been observed in neutral localized quantum dot systems like self-assembled GaAs QDs [42]. In this sample, we observed many neutral quantum dots, especially in the hole doping region. The energy splitting of these dots is around $600 \mu\text{eV}$ which is consistent with the previous studies [29, 31, 32, 43, 44]. In figure 3.4, the gate dependent PL, at -23 V gate voltage where the electron is depleted in the monolayer WSe_2 , two doublets quantum dot labeled as D3a and D3b appear simultaneously. The two quantum dots show a similar spectral wandering highlighted with red solid symbols. Because of the simultaneous appearance and identical spectral wandering, D3a and D3b are identified as originating from one quantum dot named as D3. Moreover, two more groups D2a D2b and D4a D3b have the same behavior so that they are attributed as one quantum dot D2 and D4.

Figure 3.5 is a cross-sectional PL spectrum at the specific gate voltage -78V , in which the energy difference between parent peak Da and replica Db in each group is exact 21.8 meV . In this sample, we found 6 groups of quantum dots with the properties described above shown in figure 3.6.

The 21.8 meV energy spacing is similar to the calculated $E''(\Gamma)$ phonon mode which is shown in fig 3.7.

By conducting the Raman scattering experiment of WSe_2 samples with 1-7 layers and bulk sample, the phonon mode $E''(\Gamma)$ is measured with the energy of 21.8 meV (176 cm^{-1}) which is exactly same as the energy spacing between parent dot and its replica. $E''(\Gamma)$ phonon mode is absent in monolayer as it is forbidden by symmetry constraints in Raman scattering. But as the symmetry constraint is broken by the anisotropic potential of the quantum dot, the parent

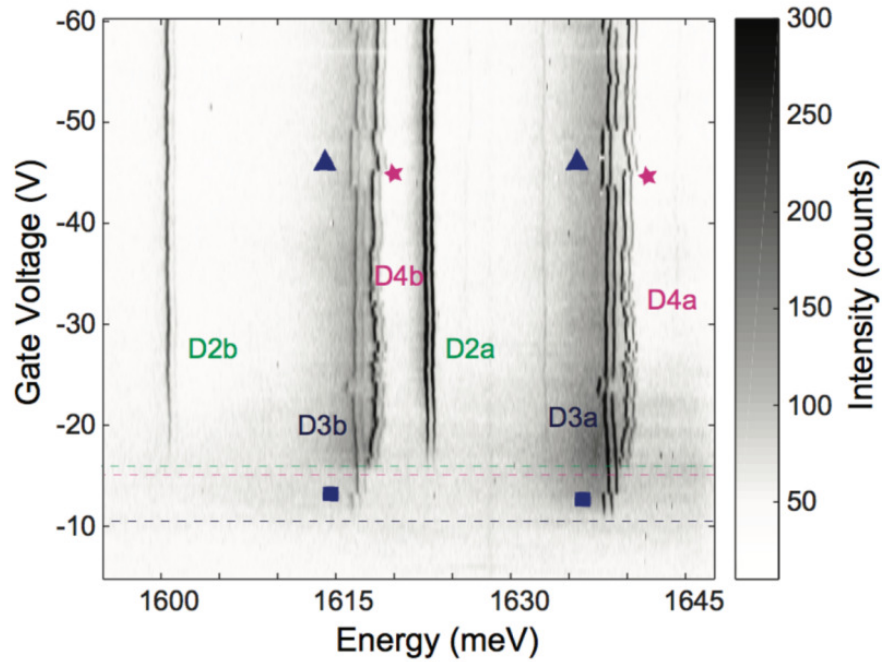


Figure 3.4: Gate-voltage dependent PL of QDs. The triangles and squares (stars) mark the spectral jittering between D3a and D3b (D4a and D4b). The dashed lines show the gate voltage where different QDs arise simultaneously.

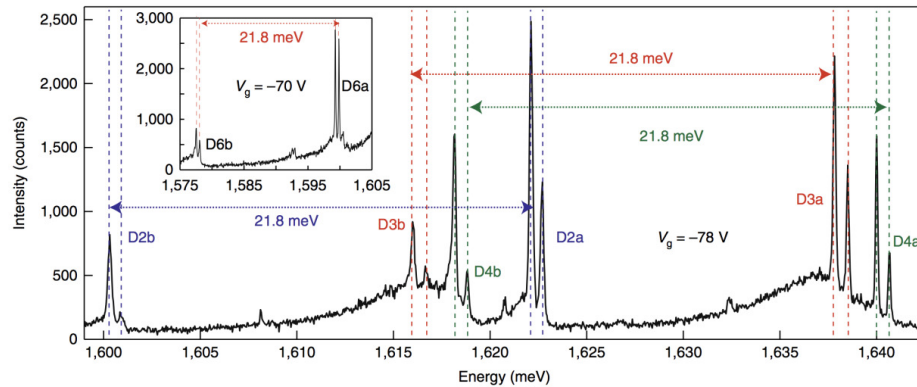


Figure 3.5: The cross-sectional PL spectrum at the gate voltage of -78 V. The splitting energies in doublet a and doublet b have the same value and the energy difference between a and b doublets is 21.8 meV for all the groups. The inset shows the PL of another doublet group at a gate voltage of -70 V.

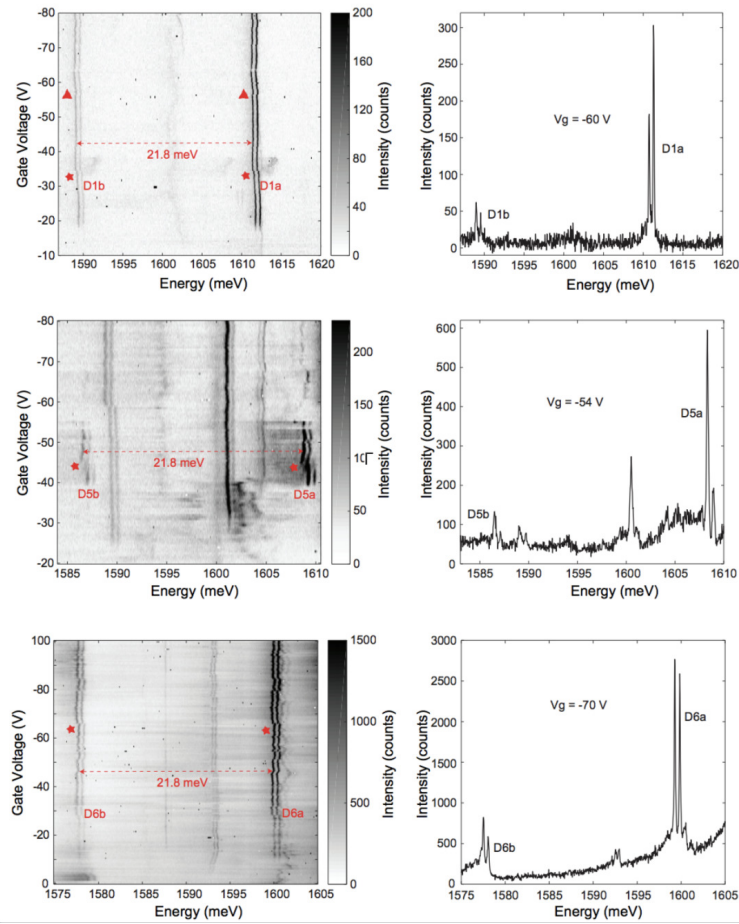


Figure 3.6: Three other doublet groups. The energy difference between doublet a and doublet b is also 21.8 meV.

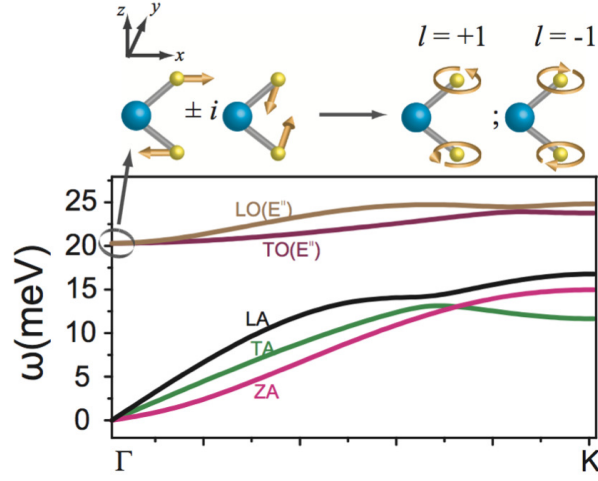


Figure 3.7: Phonon dispersion of monolayer WSe₂. At Γ -point, two optical phonon modes, LO(E'') and TO(E'') are degenerate in energy. Their oscillation modes can be combined to form two new modes. The two new modes have pseudo angular momentum (PAM) of 1 or -1.

quantum dot can interact with the E''(Γ) phonon to produce the replica peak.

The experimental observation of a Raman peak depends on the symmetry selection rules. The Raman tensor for the E'' mode in monolayer WSe₂ is [45]

$$R = \begin{bmatrix} 0 & 0 & a \\ 0 & 0 & b \\ a & b & 0 \end{bmatrix} \quad (3.1)$$

For linearly or circularly polarized light with wavevector perpendicular to the monolayer ($[1\ 0\ 0]$ $[0\ 1\ 0]$ or $1/2[1\ i\ 0]$ $1/2[1\ -i\ 0]$), the reflected light in the z direction is constantly zero as $\langle \hat{e}_z | R | \hat{e}_{excitation} \rangle = 0$. This is the reason why 176 cm^{-1} Raman mode can not be observed in the monolayer WSe₂. However, as the QDs lowers the symmetry from a threefold to twofold because of the anisotropy, the E'' phonon mode in monolayer WSe₂ can have nonzero intensity. With the increasing of the layers, the reflected light in z direction calculated as $\langle \hat{e}_z | R | \hat{e}_{excitation} \rangle \neq 0$. The Raman tensor for E_g mode in 2L

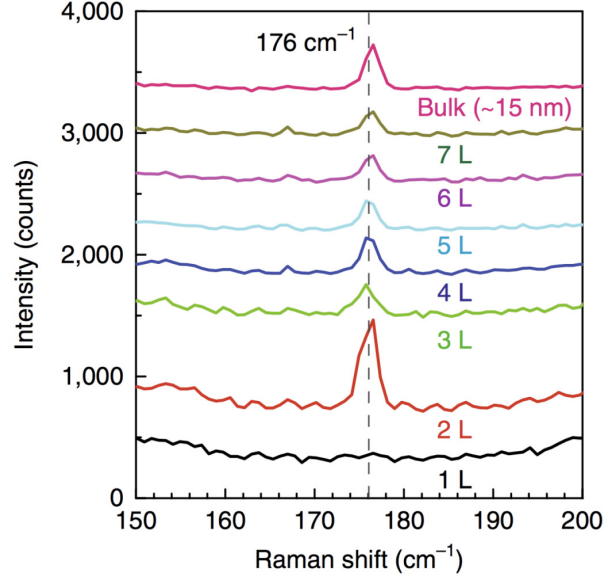


Figure 3.8: Raman scattering results in WSe_2 samples with different layers. For the WSe_2 samples with more than 2 layers, a Raman peak at 176 cm^{-1} corresponding to an energy of 21.8 meV is observed.

(4L, 6L, ...) is

$$R = \begin{bmatrix} a & c & d \\ c & -a & f \\ d & f & 0 \end{bmatrix} \quad (3.2)$$

and for 3L (5L, 7L, ...) is

$$R = \begin{bmatrix} a & c & 0 \\ c & -a & 0 \\ 0 & 0 & 0 \end{bmatrix}. \quad (3.3)$$

3.3 Power dependence and Zeeman splitting

In order to avoid other possible origins of the Db peak such as excitonic complexes, biexcitons and solid our conclusion of phonon replica, we conducted the power dependence of these quantum dots. As the QD can be regarded as a

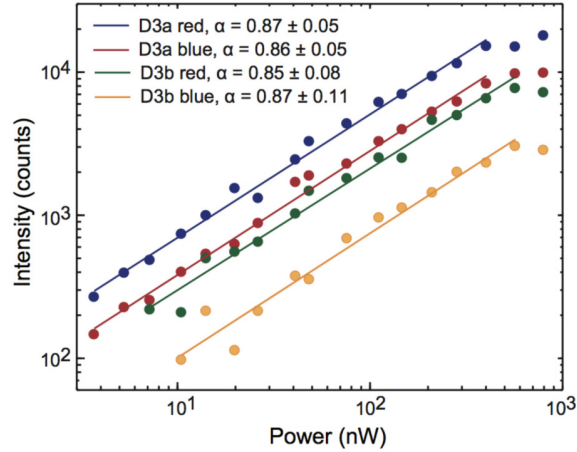


Figure 3.9: Power dependence of D3a and D3b doublet. The x-axis and y-axis are plotted in a log scale. In D3 group, the four peaks in D3a and D3b exhibit similar power dependence with a ratio of about 0.86.

two-level system different to the exciton which has a continuous band and shows a linear power dependence, the QD shows a sub-linear power dependence. In figure 6, the excitation power (P) and intensity (I) are plotted in a log scale and they have a relation $I \propto P^\alpha$ where α is around 0.8. This sub-linear power-law behavior rules out the possibility of biexcitonic origination. A similar sub-linear power law is also observed in other groups shown in figure 3.9.

Under the magnetic field applied in a Faraday configuration, both doublet peaks Da and Db exhibit a Zeeman splitting shown in the fig 3.11. By fitting the Zeeman splitting energy in a form of $E(B) = \sqrt{g^2 \mu_B^2 B^2 + \delta_0^2}$ where δ_0 is energy difference between two peaks at zero magnetic fields, the g-factor for both Da and Db peaks is approximate 9 which is consistent to previous results [29, 31, 32, 43, 44].

Furthermore, the intensity ratio between a and b peaks is about 0.2 which is also called the Huang-Rhys factor reflecting the exciton-phonon coupling intensity. This coupling intensity is about one order stronger than that in GaAs based QDs [46].

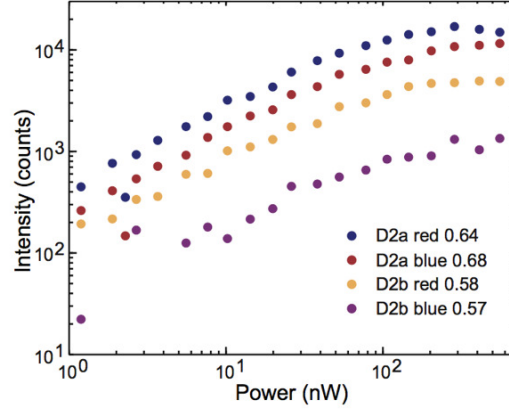


Figure 3.10: Power dependence of D2 group. In D2 group, D2a and D2b exhibit similar power dependence with a ratio of about 0.6.

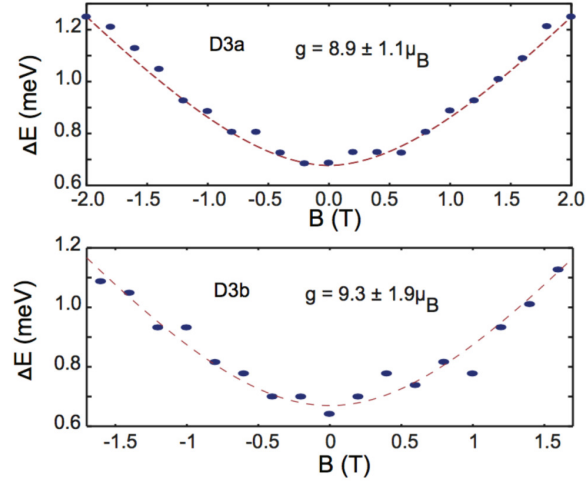


Figure 3.11: The g-factor for D3a and D3b. This figure shows the splitting energy of D3a and D3b doublets in the magnetic field. By fitting the energy difference, the g-factors are calculated with the value of $8.9 \mu_B$ and $9.3 \mu_B$.

Group	doublet \mathbf{a}	doublet \mathbf{b}
D1	9.4 ± 0.3	10.2 ± 0.6
D2	9.7 ± 0.8	9.9 ± 0.5
D3	8.9 ± 1.1	9.3 ± 1.9
D5	9.6 ± 1.2	8.6 ± 0.9

Table 3.1: g-factor of doublet \mathbf{a} and \mathbf{b} in D1, D2, D3 and D5.

Group	Huang Rhys factor
D1	0.28 ± 0.08
D2	0.32 ± 0.16
D3	0.27 ± 0.04
D4	0.88 ± 0.17
D5	0.18 ± 0.05
D6	0.26 ± 0.05

Table 3.2: Huang-Rhys factor for all the groups

3.4 Polarization measurements

As the phonon replica b peak is a result of exciton-phonon scattering from the parent a peak, information of the scattering should be reflected in the PL signal. Now we only obtain similar properties between a and b peak such as g-factor under magnetic field and power dependence. Then the polarization-resolved experiment is conducted.

In linear basis measurement that the two orthogonal linearly polarized components of signal can be separated by Wollaston prism, the polarization of the parent doublet a are shown in figure 3.12. Same as described earlier that the anisotropic electron-hole exchange splits the neutral quantum dot, the two peaks exhibit orthogonal linear polarization. In figure 3.12, the dashed line represents two ideal orthogonal linear polarization and the dot shows the experimental polarization of the two peaks in the parent dot. The experiment results fit well and therefore two peaks are orthogonal linear polarized lights.

However, the phonon replica doublet is not linearly polarized and shows a property of circular polarization or non-polarization in linear basis measurement. Then the phonon replica doublet is measured at the circular basis in which the two circular components σ^+ , σ^- are separated by Wollaston prism. The result shows that the phonon replica is completely unpolarized. The setup detail of the linear basis and circular basis is shown in the experiment method review part.

In a linear basis, the dashed lines show the behavior of the ideally linearly polarized light when we rotate the half-wave plate before the Wollaston prism. The solid red line represents the ideally circular polarization or unpolarization. In a circular basis, the green dashed line shows the behavior of the ideally circular polarization and the solid red line represents the unpolarization or

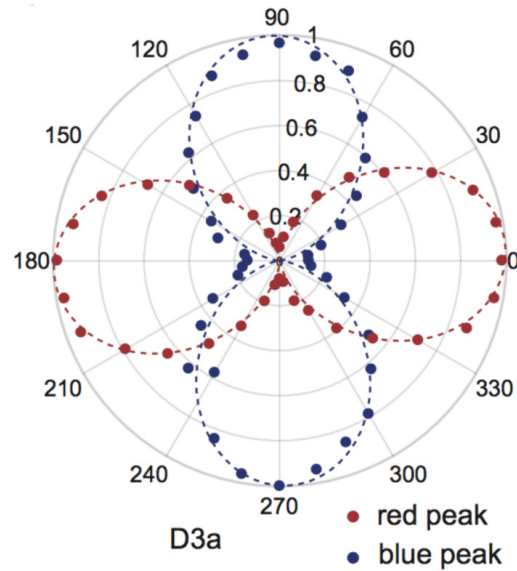


Figure 3.12: The polarization measurement results of D3a doublet in a linear basis. In a linear basis, the dashed red and blue lines represent the two orthogonal ideal linearly polarized light. The red (blue) solid dots correspond to the experimental polarization of D3a red (blue) peak.

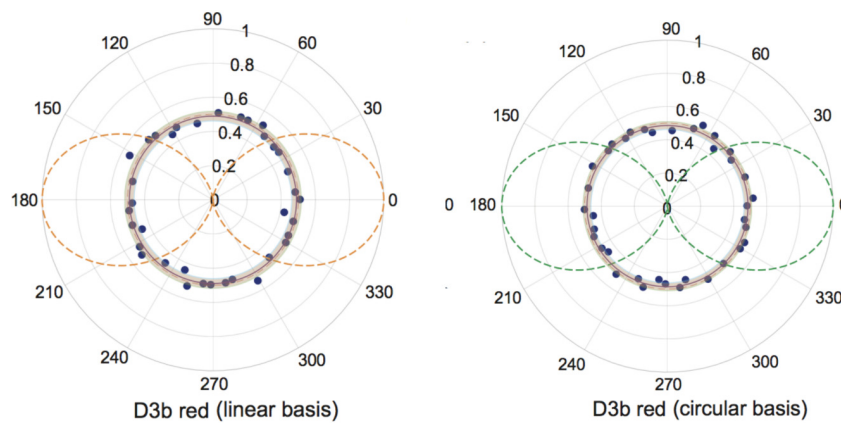


Figure 3.13: Unpolarization of the D3b red peak. The left (right) picture represents the result in a linear (circular) basis. In the linear basis, the orange dashed line represents the ideally linear polarization and the solid red line represents the ideally circular or random polarization. In the circular basis, the green dashed line represents the ideally circular polarization and the solid line corresponds to the ideally linear or random polarization. The blue dots are the experimental results for polarization measurement. Based on these measurements, the D3b red is concluded with completely random polarization.

linear polarization. Based on the experimental results, we can conclude that the D3b red peak is completely unpolarized.

In order to quantify the unpolarization of the phonon replica, we calculated its density matrix by extracting the Stokes parameters. From the polarization measurement in the linear and circular basis, we can obtain the intensities of phonon replica along horizontal (H), vertical (V), diagonal (D) and right circular (R) components from which we can calculate $n_0 = \frac{N}{2}(\langle H | \hat{\rho} | H \rangle + \langle V | \hat{\rho} | V \rangle)$, $n_1 = N\langle \bar{D} | \hat{\rho} | \bar{D} \rangle$, $n_2 = N\langle R | \hat{\rho} | R \rangle$ where N is determined by the intensity of PL and the efficiency of detector [46]. Therefore because the Stokes parameters are defined as $S_0 = 2n_0$, $S_1 = 2(n_1 - n_0)$, $S_2 = 2(n_2 - n_0)$, and $S_3 = 2(n_3 - n_0)$, the Stokes vectors can be calculated as $(\frac{S_1}{S_0}, \frac{S_2}{S_0}, \frac{S_3}{S_0})$. The density matrix is defined as $\hat{\rho} = \frac{1}{2} \sum_{i=0}^3 \frac{S_i}{S_0} \hat{\sigma}_i$ where $\hat{\sigma}_0$ is the identity operator and $\hat{\sigma}_{1,2,3}$ are the Pauli operators. In linear basis, the density matrix of ideally unpolarized state is $\hat{\rho}_{ideal} = \begin{bmatrix} \frac{1}{2} & 0 \\ 0 & \frac{1}{2} \end{bmatrix}$.

The polarization density matrix of the red peak in the

phonon replica D3b is calculated as $\hat{\rho}_{exp} = \begin{bmatrix} \frac{1}{2} & 0.014 + 0.007i \\ 0.014 - 0.007i & \frac{1}{2} \end{bmatrix}$.

Therefore the fidelity of D3b red peak is $F = Tr(\sqrt{\sqrt{\hat{\rho}_{ideal}}\hat{\rho}_{exp}\sqrt{\hat{\rho}_{ideal}}}) = 0.999 \pm 0.016$. The fidelity value is very close to one and therefore demonstrates the unpolarization of the phonon replica.

The polarization measurements of D4 group in both linear and circular basis are shown in figure 3.14. The D4a doublet are orthogonal linear polarized and the D4b red peak is unpolarized. The density matrix of D4b red peak's polarization is calculated as $\hat{\rho}_{exp} = \begin{bmatrix} 0.506 & 0.009 - 0.005i \\ 0.009 + 0.005i & 0.494 \end{bmatrix}$ and the fidelity is 0.999 ± 0.013 . The polarization density matrix is plotted in figure

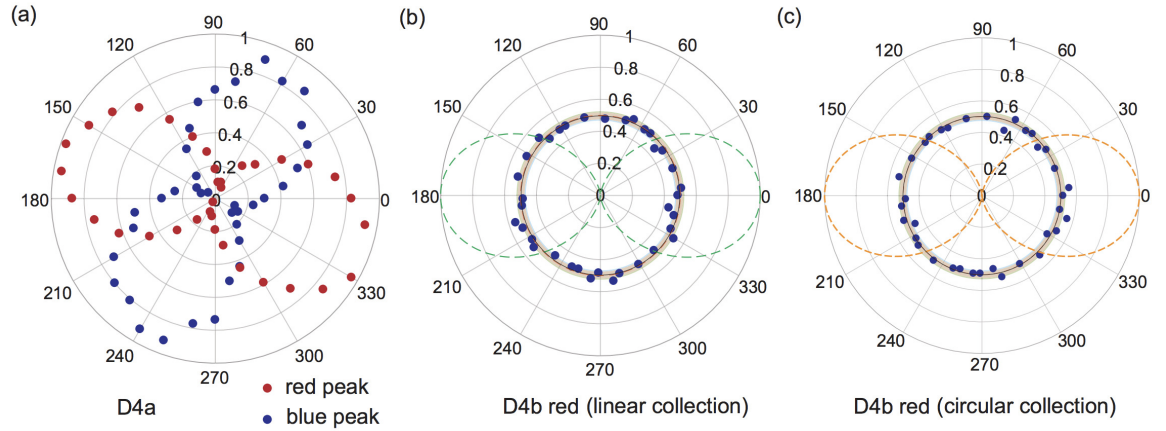


Figure 3.14: Polarization measured in both linear and circular basis. D4a doublet is orthogonal linearly polarized and D4b red peak is unpolarized.

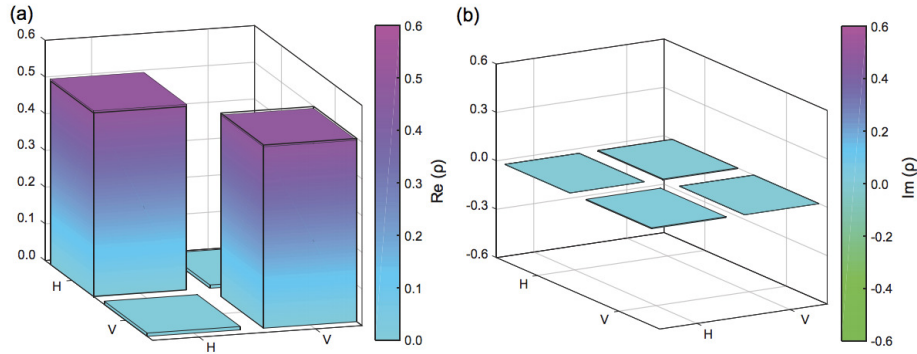


Figure 3.15: Real and imaginary parts of the density matrix of D4b red peak. The diagonal value of 0.5 in the matrix of real parts shown in the left picture corresponds to a completely mixed state.

3.15.

3.5 Single photon and chiral phonon entanglement

Comparing the linear polarization of parent doublet Da and un-polarization of phonon replica Db, it seems that the linear polarization of Da is lost during the photon-phonon scattering process. Meanwhile, the phonon replica can

inherit the properties of power dependence and g-factor from the parent peak. These behaviors of phonon replica raise a puzzling question that what happened during the coherent Raman scattering process.

To explain this un-polarization, the $E''(\Gamma)$ phonons involved should be investigated first. In the phonon dispersion, at Γ -point, there is a doubly degenerate phonons which can be combined to form two orthogonal chiral phonon with pseudo angular momentum (PAM) ± 1 [47]. These chiral phonons [47] are recently proposed and experimentally observed [49]. Due to the threefold symmetry, the phonon-photon scattering process should satisfy the selection rule of PAM conservation that the angular momentum change between scattered photon and initial photon should be equal to the PAM of chiral phonon involved. Constrained by this selection rule, the chiral phonon with PAM $+1$ (-1) can only couple a σ^- (σ^+) photon to produce a scattered photon with the angular momentum of $+1$ (-1). As each linear polarized peak can be regarded as a superposition of σ^+ and σ^- photons with equal weight, following the selection rule, the two indistinguishable scattering paths in this "which-way" scattering process from one parent peak to the corresponding phonon replica peak lead to an entanglement state.

Consequently, the Raman scattering process produces a maximally entangled state consisting of the combined emitted phonons and scattered photons system shown in 3.16. The entangled state can be written as $|\psi_{tot}\rangle = \frac{1}{\sqrt{2}}(|\sigma^+\rangle \otimes |l = +1\rangle \pm i |\sigma^-\rangle \otimes |l = -1\rangle)$. Because only the photon information is measured and the phonon information is not accessed in our experiment, the density matrix of one replica peak state is acquired by tracing out the phonon subsystem as $|\psi_{photon}\rangle\langle\psi_{photon}| = \frac{1}{\sqrt{2}}(|\sigma^+\rangle\langle\sigma^+| + |\sigma^-\rangle\langle\sigma^-|)$ which is a completely unpolarized state independent of the measurement basis. In the other

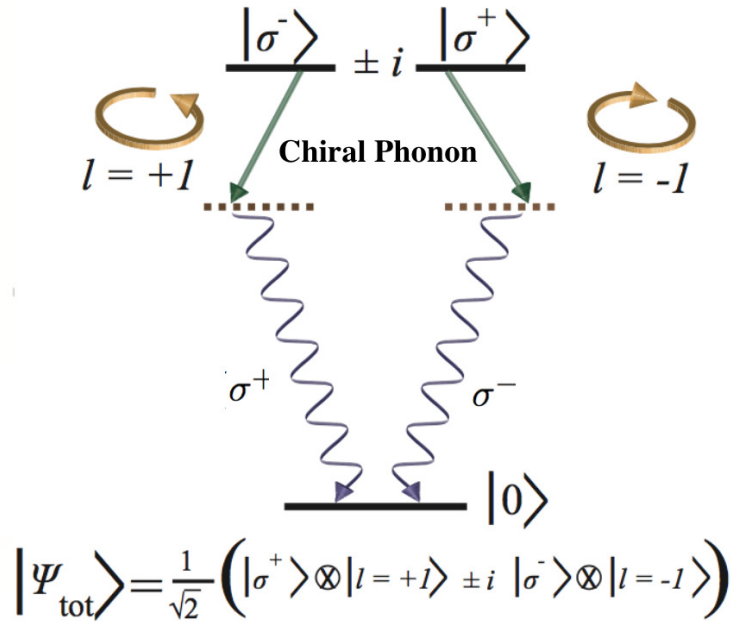


Figure 3.16: Schematic of entanglement between single photons and chiral phonons. The chiral phonons with PAM of +1 and -1 are degenerate and the left and right circularly polarized lights are also degenerate due to the time-reversal symmetry. From the selection rules of the chiral phonon, the left (right) circularly polarized photon can only couple to chiral phonon with PAM of +1 (-1) to produce a scattered photon with the right (left) circular polarization. As the two scattering process are indistinguishable, the scattering process can be present as an entanglement state.

aspect, once the chiral phonon PAM information $l=+1$ or -1 is measured, the polarization of photon can be simultaneously projected to σ^+ or σ^- . However, it is challenging to measure the emitted phonon which has a lifetime of tens picoseconds and decays to other modes with the lower energy due to anharmonic lattice potential [50].

3.6 Polarization recovery under magnetic field

The entanglement we claimed above is extremely dependent on two sets of energy degeneracy protected by time-reversal symmetry of σ^\pm and orthogonal $E''(\Gamma)$ chiral phonons with PAM ± 1 . Once one of the degeneracies is broken, the entanglement is destroyed. Although the chiral phonons in the non-magnetic WSe₂ monolayer do not couple to the magnetic field, the magnetic field can break the energy degeneracy of σ^\pm .

The figure 3.17 shows the behaviors of both the parent dot a and phonon replica b under the perpendicularly applied magnetic field. By increasing the magnetic field, the two peaks in parent dot recover circular polarization as the exchange interaction between K and -K valley is overwhelmed and meanwhile, the two peaks of phonon replica also exhibit circular polarization.

As the chiral phonon emitting process is not affected by a magnetic field, this polarization recovery of the phonon replica confirms our entanglement claim and it excludes other possible mechanisms such as a random scattering process. In such a process, the polarization of the phonon replica is oriented at a random angle then the polarization of the parent dot is lost. The pseudo angular momentum selection rule requires a polarization reversal between the chiral phonon $E''(\Gamma)$. This helicity change is observed in the non-resonant

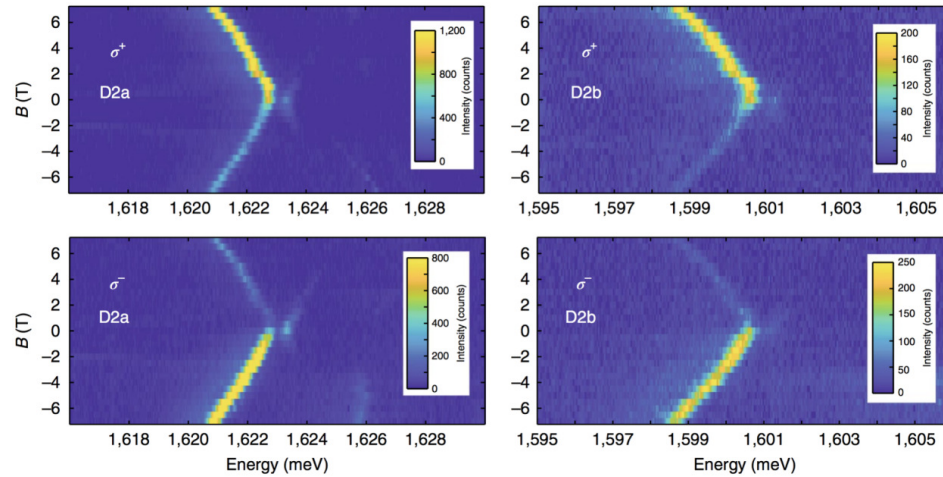


Figure 3.17: The polarization of D2a and D2b in an out-of-plane magnetic field. The D2a and D2b peaks recover right (left) circular polarization under positive (negative) magnetic field.

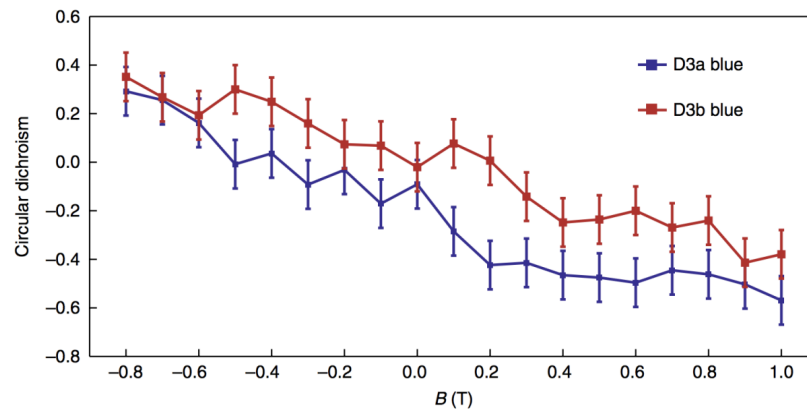


Figure 3.18: Circular dichroism under different magnetic fields for D3a blue and D3b blue peaks.

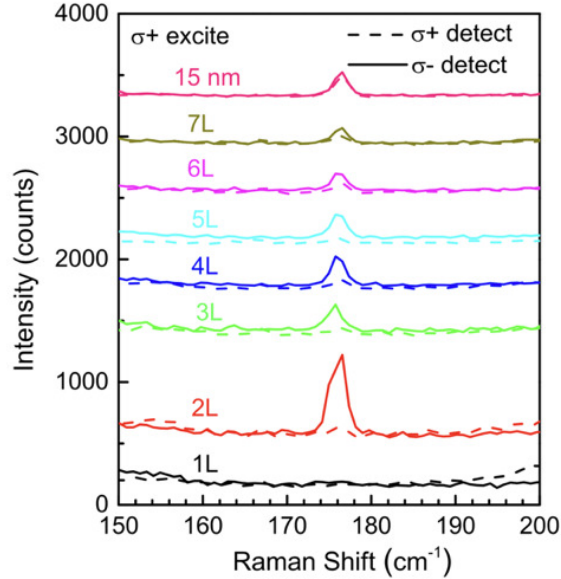


Figure 3.19: Helicity-resolved Raman scattering measurement of E'' ($E_g/E'/E_{1g}$) mode under non-resonant excitation. The polarization of the incident laser is σ^+ . E_g/E' mode exhibit σ^- polarization from 2-5L WSe_2 and only with a small component of σ^+ . For 6L, 7L and bulk (15nm), the opposite polarization effect becomes weaker. The excitation laser has a wavelength of 446.1 nm and 0.5 mW.

Raman scattering experiment shown in figure 3.19. In the monolayer WSe_2 , the E'' transforms like $(x + iy)z$ and $(x - iy)z$. The counterpart of the E'' in monolayer WSe_2 is E_g mode in even-layered WSe_2 . In odd-layered WSe_2 , the E'' mode in monolayer WSe_2 splits into E'' and E' mode.

From the entanglement scheme between the chiral phonons and photons, the scattered photon and the emitted photon should have different helicities. In our experiment, the parent peak and its corresponding phonon replica exhibit a co-polarization under the finite magnetic field. We lack the understanding of the helicity behavior and need further research to solve this puzzle. Similar helicity behavior is also observed in other groups that the helicity of the Raman scattered photon is reversed with respect to the incident photon when the

incident light is far tuned to the exciton energy, but under quasi-resonant excitation condition, they become co-polarized. In our case, the parent peak plays a role of the laser in a Raman scattering experiment and the phonon replica acts in the scattered Raman peak. The parent quantum dot's wavelength plays the role of the free exciton's wavelength in Raman scattering experiment so that the excitation energy of the entanglement picture is exact a resonant Raman scattering process which leads the co-polarization consistent with previous works [76–78].

The observed strong coupling between quantum dots and chiral phonons can serve as a single source of chiral phonons.

3.7 PLE & localization of QDs & Raman symmetry analysis

3.7.1 PLE

The Photoluminescence excitation spectroscopy (PLE) measurements are conducted for D2a, D3a and D4a doublets with a laser tuned from the low energy side to the high energy side. For D3a and D4a doublets, a prominent peak appears with energy about 53 meV larger than the emission which could be the 2s state of the QD [43, 51] shown in 3.20.

3.7.2 Localization of QDs

Because the quantum dots are believed as localized excitons, therefore, a spatial scanning of the QDs' PL is conducted in the region of the dashed square marked in figure 3.21(a) whose size is about $16 \times 16 \mu m^2$. And the region of the doublet

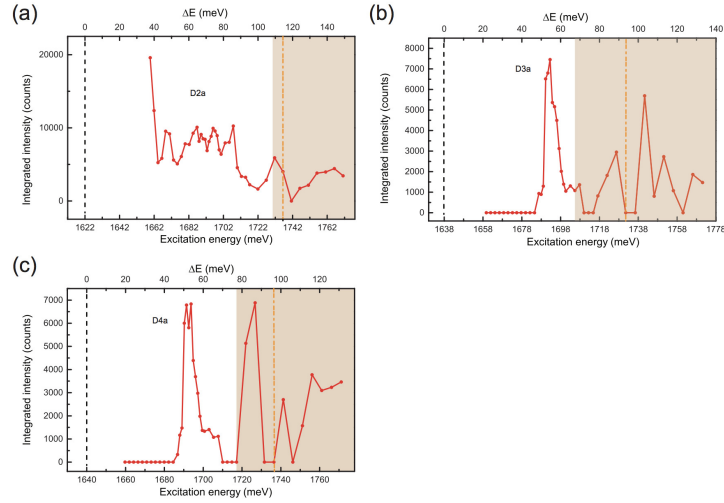


Figure 3.20: PLE of D2a D3a and D4a doublet. The black dashed line marks the emission energy of the doublet and the orange dash-dot line indicates the free exciton's energy. As the excitation energy increases, the defect states exhibits a broad background in the spectra which is marked as the brown shaded regions. The extracted PLE in the shaded region can not fully reflect the PLE. However, the prominent peak with 53 meV higher energy than the doublet peak indicates the 2s state of the QD.

D2a, D3a, D4a and D6a are shown in the figure 3.21(b)-(e). From the scanning result, it is clear that all these QDs are localized. As the spot size of excitation laser is about $1 \mu\text{m}$, the quantum dot's intensity can be observed in a large region at the level of μm which is not the real size of quantum dots. For a quantum dot in monolayer WSe_2 with a large phonon sideband, by adopting the deformation coupling between acoustic phonon and quantum dot, the size of a quantum dot in the monolayer WSe_2 we have calculated is about 4nm which will be described in Chapter 5.

3.7.3 Raman symmetry analysis

As described before that in monolayer WSe_2 , the E'' phonon mode is can not be observed. The Raman tensor for the E_g mode in 2L (4L, 6L,...) WSe_2 can be represented as [45]

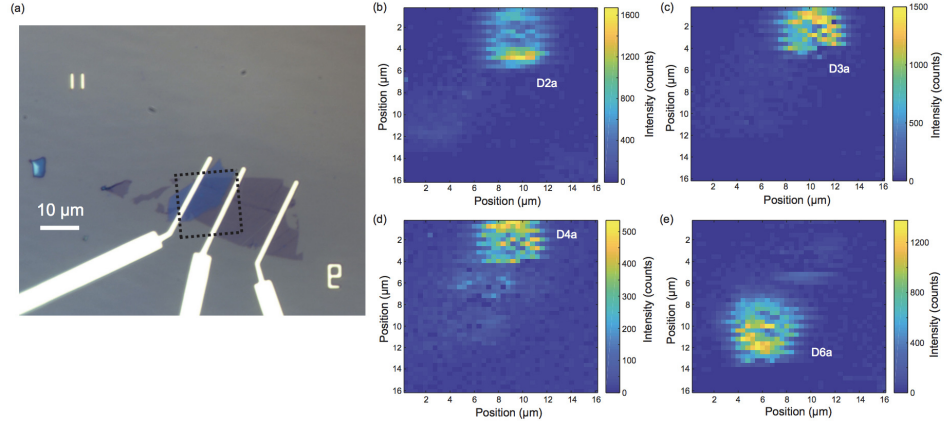


Figure 3.21: Spatial localization of the QDs in the monolayer WSe₂ FET device. Figure a shows the sample under an optical microscope. The dashed square marked in figure a indicates the scanning region whose size is about $1 \times 16 \mu\text{m}^2$. b-e shows the PL intensity map of D2a red peak (1662.4meV), D3a red peak (1638.2meV), D4a red peak (1640.2meV) and D6a red peak (1599.3meV). During the spatial scan, the gate voltage is -80V and the excitation wavelength is 732.5nm with the power of 300nW.

$$R = \begin{bmatrix} a & c & d \\ c & -a & f \\ d & f & 0 \end{bmatrix} \quad (3.4)$$

and Raman tensor for the E' mode in 3L (5L, 7L,...) can be represented as

$$R = \begin{bmatrix} a & c & 0 \\ c & -a & 0 \\ 0 & 0 & 0 \end{bmatrix} \quad (3.5)$$

Because of the symmetry, the reflected emission should have opposite polarization compared to the incident excitation. From figure 3.19, the observed reflected light has the polarization $(I_+ - I_-)/(I_+ + I_-)$ with a value of nearly -100% where negative value means the opposite chirality of the Raman emission. The

selection rule is relaxed in thicker few-layer (6L and 7L) and bulk (15L). The Raman tensor for the bulk is the same as the monolayer so that the E_{1g} mode should not happen. However, the E_{1g} mode exhibits both σ^+ and σ^- with similar intensities.

In this chapter, by studying the properties of QDs in a field-effect transistor, two doublets are observed from the same QD and they exhibit a correlated spectral jittering, power dependence, and g-factor at magnetic fields. More importantly, we have observed the entanglement between chiral phonons and single photons. The strong phonon-photon interaction can serve as a source of chiral phonon and lay the groundwork for the realization of the quantum-optomechanics platforms in 2D materials.

3.8 Conclusion and Perspectives

We report the entanglement between single photons and chiral phonons in monolayer WSe_2 . The entanglement can serve as a source for generating single chiral phonon and the strong exciton-phonon coupling between the QDs and chiral phonons lay the ground for the optomechanical platform. Further research can exploit the chiral phonon coupling to control and manipulate the quantum states of the QDs. It is challenging and also intriguing to study the entanglement state by directly measuring the chiral phonon.

Chapter 4

Optical initialization of quantum dot with a single spin-valley

Control and manipulation of the charge's internal properties at a single particle level are valuable for applications in fields such as quantum information, spintronics and so on [52, 53]. Atomically thin TMD materials provide a promising platform for studying a single charge's spin and valley with various possible experimental methods as electrical, magnetical, and optical controls. In this work, we achieved the optical initialization of a single spin-valley in a single hole under a small magnetic field. In other words, a single spin-valley state is selectively produced by circularly polarized light with different helicities.

4.1 Single spin-valley control mechanism

QDs in the monolayer WSe₂ are believed to be localized excitons trapped in potential wells produced by strains or defects [30, 54, 55]. As the valley properties of excitons are preserved in the QDs, the confinement of potential wells

should be larger than the Bohr radius of excitons and trions whose length scale is about 1-2 nm [56] and it is safe to use the single-particle band structure.

In neutral QDs, the anisotropic exchange interaction mixes two exciton states at K and -K valley and then splits the neutral QDs into two peaks. But for the trion configurations, the results of the exchange interaction is different.

In a negatively charged bright exciton with one pair of electron and hole at the same valley having the same spin, the two electrons have two configurations located at the same valley or different valley shown in figure 4.1.

The exchange interaction J_{eh} between the electron and hole in the exciton mixes the two configurations and the exchange interaction between the hole and excess electron splits the two configurations [34, 57]. However, for the single positively charged excitons, due to the large spin-orbital splitting in the valence band, the exchange interaction can not mix or split its states. Because of the large spin-orbit splitting, the two holes can only be located at two different valleys shown in figure 4.1. If the exchange interaction between electron and hole in one exciton happens, two holes with the same spin are located in one valence band which is blockaded by the Pauli principle as figure 4.1 shows.

The other exchange interaction between the excess hole and electron is suppressed because the energy splitting in the valence band is large. As the lifetime of the free holes at the order of microseconds [58–62] is much longer than the lifetime of the free excitons (orders of picoseconds) and quantum dots (orders of nanoseconds), under the condition of exchange interaction quenching, the spin-valley information can be preserved for a longer time. Therefore, the single hole with a locked spin-valley state is initialized by helicity dependent excitation laser.

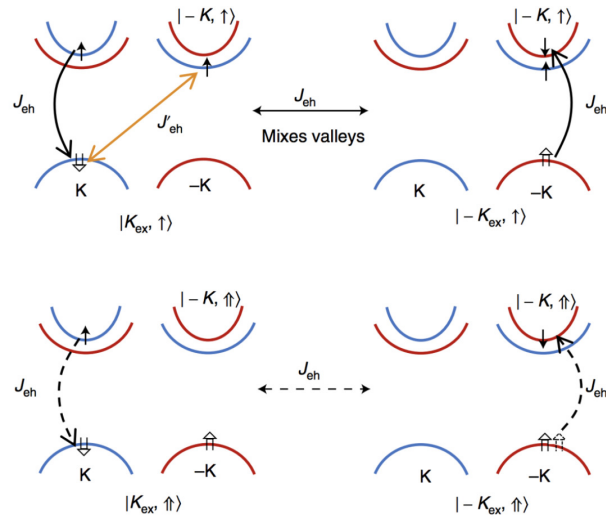


Figure 4.1: Schematic illustration of single-particle states comprising two (one) electron and one (two) holes. The top part represents the two bright configurations of the negatively charged trion that one electron and one hole are located in the same valley with the same spin and the other electron are located in the same valley or opposite valley. The long-range exchange interaction between the electron and hole in the same valley with the same spin mixes the two configurations. But for the single positively charged trion shown in the bottom part, the long-range exchange interaction is strongly suppressed by Pauli blocking as the long-range exchange interaction leads to two holes located at the same valley with the same spin. The blue (red) line means the electron band with spin up (down).

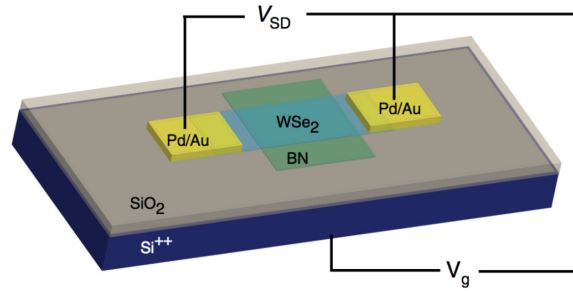


Figure 4.2: Schematic of monolayer WSe₂ field-effect transistor device. The monolayer WSe₂ sample is above a few-layered BN. Changing V_g can control the doping level in the monolayer.

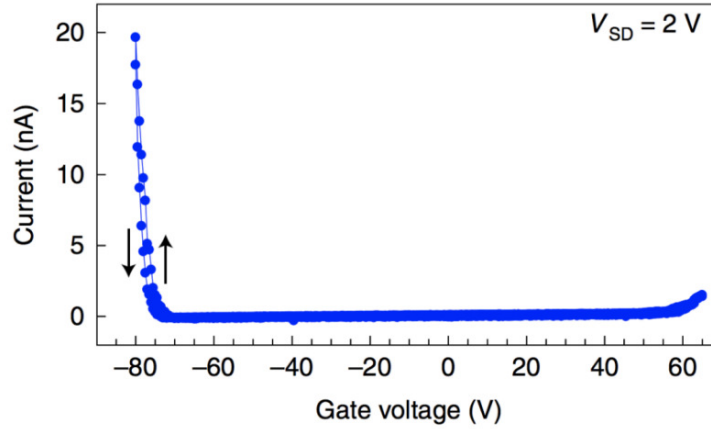


Figure 4.3: The FET current I_{sd} at different gate voltages measured with a source-drain voltage of 2V. The arrows indicate forward or backward sweeps.

4.2 Positively charged quantum dot

The field-effect transistor device of monolayer WSe₂ is plotted in a cartoon as shown in figure 4.2 and it exhibits a bi-polar behavior when applying an electrostatic doping shown in figure 4.3.

As the hole current at a negative gate voltage is stronger than the electron current at the positive gate voltage, this FET device has a higher propensity for hole-doping than electron doping. At the negative voltage region, significant holes are injected into the monolayer WSe₂ which provides a source to combine

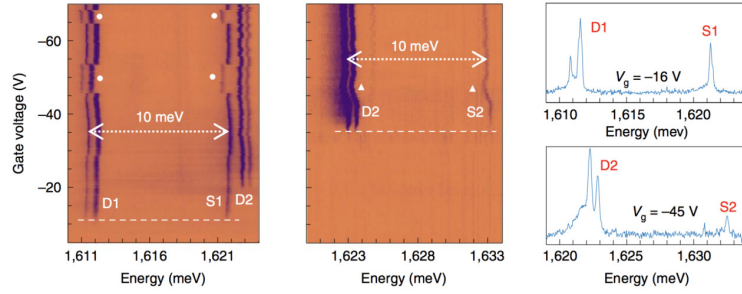


Figure 4.4: PL intensity at different gate voltages and the cross-sectional PL spectra at a specific gate voltage in the PL maps on the left. D1/S1 or D2/S2 appear at the same gate voltage and have the same spectral jittering. The energy difference between singlet and doublet in each group is around 10 meV.

with excitons to form positively charged excitons and the positively charged quantum dots.

The gate voltage V_g dependent PL measurement is performed by exciting with a low power incident laser (about 400 nW) whose wavelength is tuned to make the quantum dot's signal maximum. Figure 4.4 shows several quantum dots' peaks, one singlet and two doublets. As the singlet labeled as S1 and doublet labeled as D1 appear simultaneously at the gate voltage around -10 V and have identical spectral wandering, we can conclude that they originate from the same quantum dot. Similarly, another group consisting of one singlet (S2) and one doublet (D2) is found to be from one quantum dot as they exhibit the same behaviors as S1 and D1.

The energy difference of the doublet is about $600 \mu\text{eV}$ consistent with the fine structure splitting of neutral quantum dots studied in previous research. We attribute the doublet to a neutral quantum dot. The binding energy between the singlet and doublet is about 10 meV which might originate from the Coulomb interaction and the details of wavefunction in the local potential of each quantum dot. As described above that the exchange interaction in a positively charged quantum dot is quenched, the two optically bright exciton

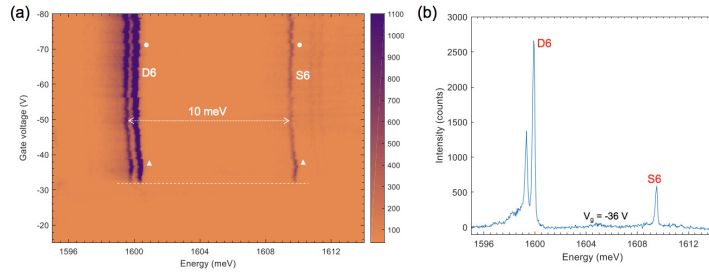


Figure 4.5: PL intensity at different gate voltage and the cross-sectional PL spectra at a specific gate voltage in PL maps on the left. D6 and S6 appear at same gate voltage and have the same spectral jittering. The energy difference between singlet and doublet in each group is around 10 meV.

states are degenerate with no splitting. And considering that these singlets only appear at the hole doping region, we conclude that the singlet is a single positively charged quantum dot state. The recently discovered negatively charged quantum dots [63] in WSe_2 show energy splitting different to the positively charged dots because of the electron-hole and electron-electron exchange interaction described earlier which leads to an energy splitting. In figure 4.7, the charged singlet shows a similar power dependence as the neutral doublet. They exhibit a similar ratio and have an origination from the same quantum dot.

In the gate voltage-dependent PL spectroscopy measurement, the integration time of each spectrum is tens of seconds. The coexistence of single positively charged states and neutral states indicate a faster release and capture time of the excess hole by the localized neutral exciton. In figure 4.8, the anti-correlation of their intensity corroborates our claim of the same QD origination.

As shown in figure 4.8, once the intensity of the singlet becomes stronger, the doublet intensity becomes weaker, and vice versa, this intensity change indicate that the trapped hole is dynamically captured and released.

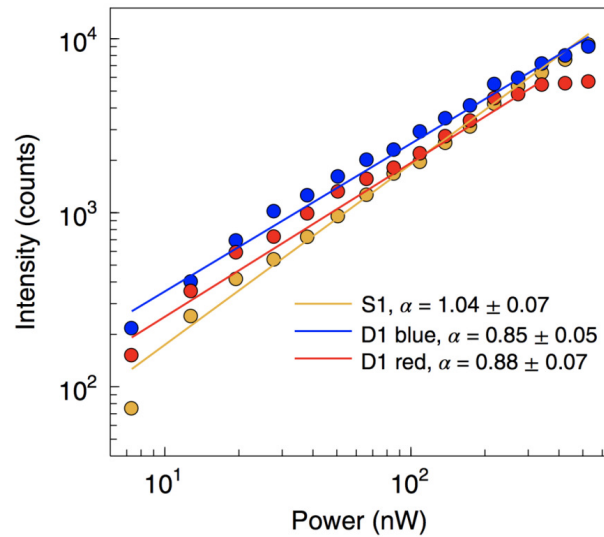


Figure 4.6: Power dependence of S1/D1 group. The intensity and power axes are plotted on a log scale. The lines fit the sublinear power-law that I is proportional to P^α .

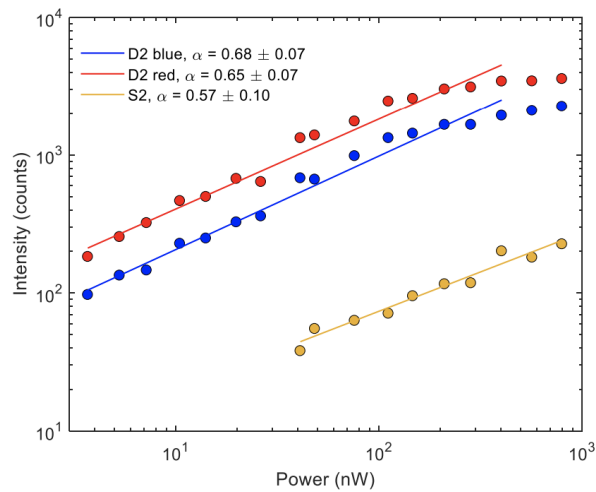


Figure 4.7: Power dependence of S2/D2 group. The intensity and power axes are plotted on a log scale. The lines fit the power law, I proportional to P^α .

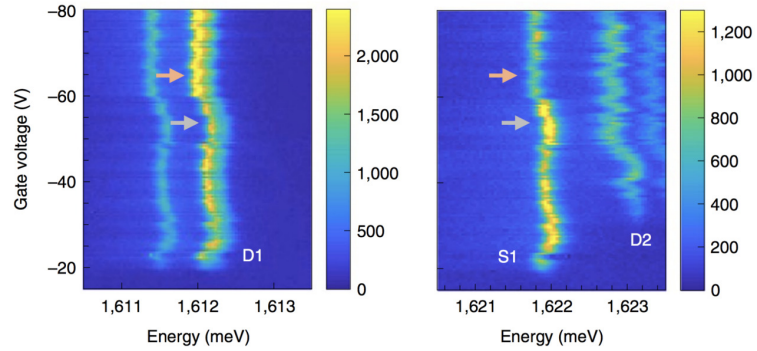


Figure 4.8: Intensity correlation between D1 and S1. Marked by the orange (grey) arrow, when D1 intensity becomes stronger (lower) the S1 intensity becomes weaker (stronger).

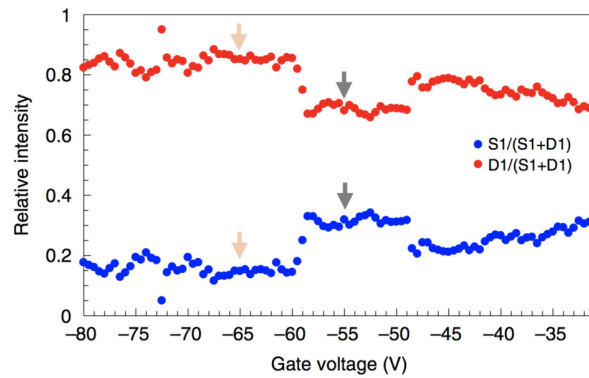


Figure 4.9: The extracted relative intensity of S1 (blue dots) and D1 (red dots). The wavelengths of the excitation laser for S1/D1 and S2/D2 are 735 nm and 747 nm.

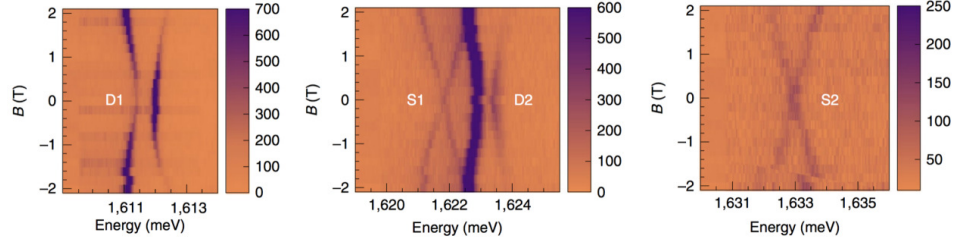


Figure 4.10: PL maps of S1/D1 and S2/D2 groups under different magnetic fields.

Group	X_d^+	X_d^0
S1-D1	12.9 ± 0.1	9.8 ± 0.2
S2-D2	12.9 ± 0.2	9.9 ± 0.2
S6-D6	13.0 ± 0.3	9.4 ± 0.5

Table 4.1: g-factors for the singlets and doublets in three groups.

4.3 Polarization resolved magneto-optical measurement

By applying a magnetic field in the Faraday configuration to the monolayer WSe₂, the single positively charged peak splits into two peaks with an X shape and the neutral dot exhibits an increasing fine structure. The extracted g-factors for single positively charged peaks are approximately 13 larger than neutral peaks' about 10 consistent to previous results [29, 31, 32, 44]. It is also consistent with the trend that the positively charged free exciton has a larger g-factor than the neutral free exciton [64]. The reason for the g-factor difference is the Coulomb interactions between the electron and holes in the charged quantum dot state. Table 4.1 shows the g-factor summary of the singlet and doublet in three QD groups.

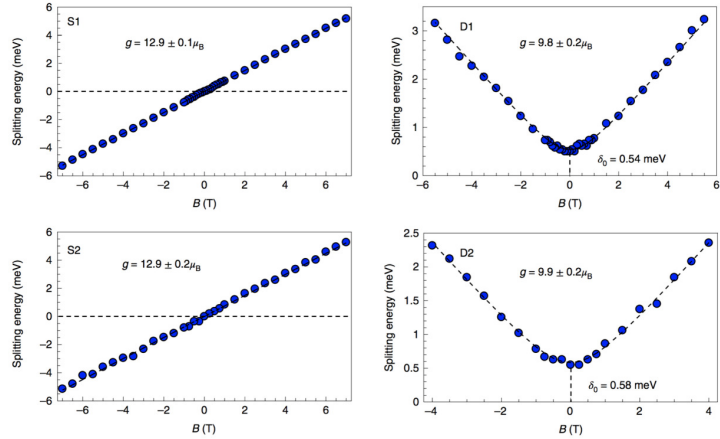


Figure 4.11: The splitting energy of S1, D1, S2, and D2. By fitting the splitting energy difference, the g-factors for singlet are around 13 and for doublet is around 10. The energy difference of the doublet under zero magnetic field is about 0.5 meV consistent with previous studies.

As the relaxation time is much shorter than the recombination time, at the high magnetic field, the red peak intensity of the neutral dot X^0 is larger than the blue peak's intensity due to thermalization. However, the intensities of two peaks in charged dot X^+ have comparable intensity indicating that the magnetic split initial states of X^+ before recombination should have similar energy. This is qualitatively consistent with the X^+ configuration in the single-particle picture that the energy splitting in exciton's electron-hole pair of X^+ is compensated by the opposite energy changing of the excess hole in X^+ so that the two states of X^+ have similar energy which then leads to a comparable PL intensity.

The neutral dots exhibit an orthogonal linear polarization at zero magnetic field induced by the exchange interaction and a circular polarization at the high magnetic field. However, the single positively charged quantum dot shows different behaviors. The excitation laser used is about 33 meV blue-detuned with respect to the energy of the single positively charged QD at zero magnetic field. The polarization is analyzed by defining a parameter named as the degree

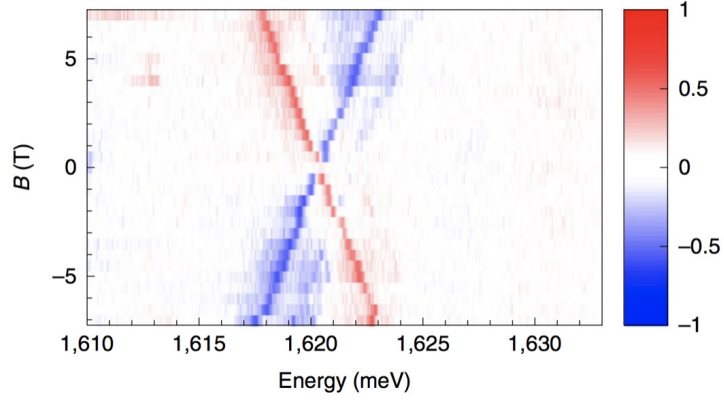


Figure 4.12: Color plot of DCP $(I_{\sigma+}-I_{\sigma-})/(I_{\sigma+}+I_{\sigma-})$ under the linear excitation. At zero magnetic field, the singlet does not have a circular component but the DCP increases when the magnetic field is increasing.

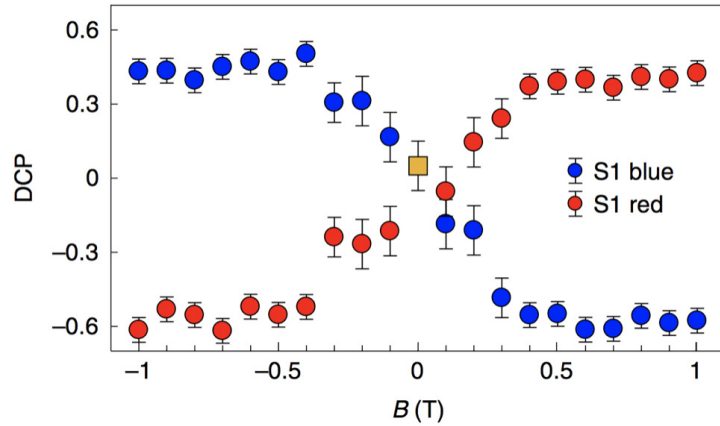


Figure 4.13: DCP of the two split peaks of S1. At even a low magnetic field about 0.5 T or -0.5 T, the two peaks recover sizeable circular components.

of circular polarization (DCP) as $\frac{I_{\sigma+}-I_{\sigma-}}{I_{\sigma+}+I_{\sigma-}}$ where $I_{\sigma\pm}$ denotes the intensities of left or right circular polarization. As zero magnetic field, the two states $|K_{\uparrow}\rangle$ and $| -K_{\downarrow}\rangle$ are degenerate and thus the single peak of singly positively charged dots is unpolarized. The DCP measured at zero magnetic field has a vanishingly small magnitude in the circular measurement basis. Combining the polarization results measured in linear basis shown in figure 4.14, it is unpolarized at zero magnetic field.

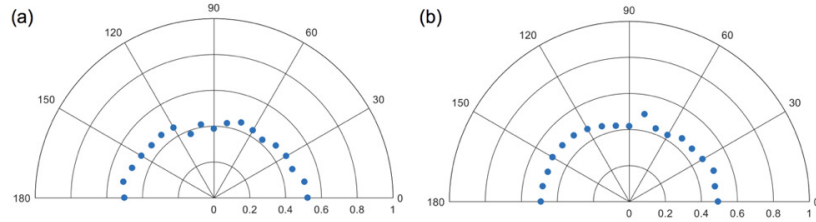


Figure 4.14: Polarization of S1 and S2 measured in a linear basis. The intensities of S1 and S2 do not change when the polarizer is rotated. Combining the 0 DCP value measured at zero magnetic field, the singlet is unpolarized.

By increasing the intensity of the magnetic field, the value of DCP becomes larger up to around 0.6 implying that the two split peaks recover circular polarization. This circular polarization recovery is a result of the valley Zeeman effect [56, 64, 65] between the two exciton states at K and -K valley. After the recombination process, the X^+ and X^- emit σ^+ and σ^- polarized photons with different energies under the finite B leaving an excess hole in -K or K valley. Shown in figure 4.14, the DCP has sizeable magnitude even at a low magnetic field about 0.3 T as a result of the exchange interaction quenching between the $|K_{\uparrow}\rangle$ and $| -K_{\downarrow}\rangle$ states and DCP gets saturated when B is above 0.5T.

4.4 Single spin-valley initialization

The disappearance of the exchange interaction between the two states $|K_{\uparrow}\rangle$ and $| -K_{\downarrow}\rangle$ and the expected long lifetime of the excess hole raises the possibility to control each state by the excitation light with different helicities and consequentially to control an excess hole with specific spin-valley index in each state. Applied with a perpendicular magnetic field, the singlet S2 shows different emissions with different circularly polarized excitation lights. Under σ^+ (or σ^-) excitation, only σ^+ (or σ^-) emission branch is observed indicating the

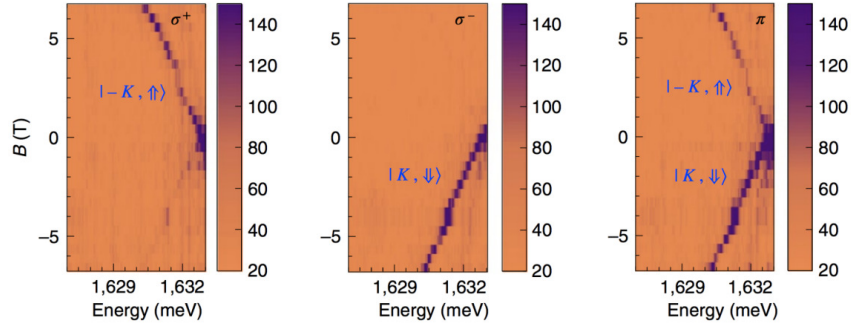


Figure 4.15: The PL intensity maps of S2 under a perpendicular magnetic field. With σ^+ , σ^- or a linearly polarized light as excitation, the PL of S2 exhibits different peaks. Under σ^+ (σ^-) excitation, only σ^+ (σ^-) emission is observed. Under the linear polarized excitation, both peaks are observed.

recombination process leaves a correlated excess hole $| -K_{\uparrow} \rangle$ (or $| K_{\downarrow} \rangle$). And when the excitation light is linearly polarized (π), both branches with σ^+ and σ^- emissions are observed. Considering the fact that the excess hole in each positively charged trion states located in the opposite K valley compared to the recombined electron and holes, we conclude that the single hole with a specific spin-valley index can be initialized by controlling the helicity of the excitation laser.

The strength of the single spin-valley's initialization is quantified by the parameter $\frac{I_{B^+} - I_{B^-}}{I_{B^+} + I_{B^-}}$ and the strength at different B shown in figure 4.16. The ratio with a value of 50% at 0.5 T approaches to approximate unity implying strong initialization.

Remarkably, the single spin-valley hole can be initialized even under a small magnetic field such as 0.1 T as long as the two splitting peaks can be distinguished in the spectra.

This co-polarization between the excitation and emission light in positively charged exciton states does not exist in the neutral quantum dot shown in figure 4.19. No matter exciting with linearly or circularly polarized lights, the

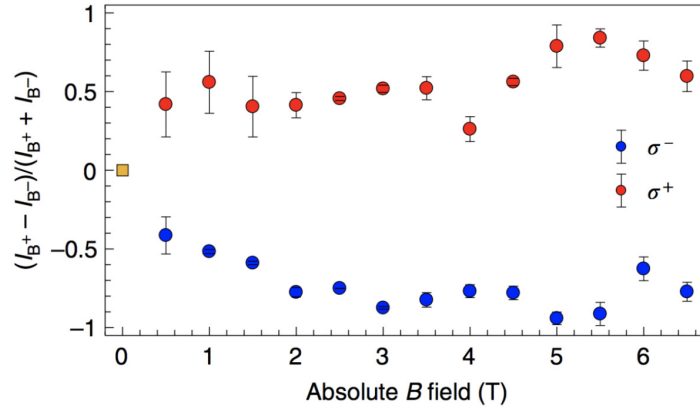


Figure 4.16: Extracted B dependent ratios, $(I_{B^+} - I_{B^-}) / (I_{B^+} + I_{B^-})$ of the S2 red peak, where I_{B^+} (or I_{B^-}) denotes the positive (or negative) magnetic field. At the high magnetic field, the ratio approaches to nearly 1 implying almost completely optical initialization of the spin-valley state.

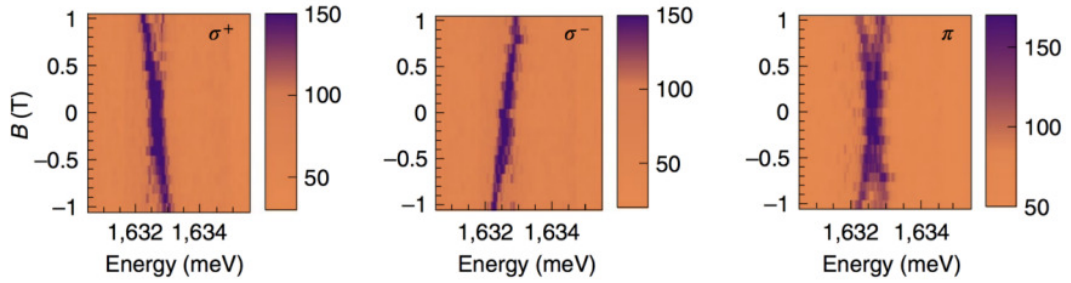


Figure 4.17: PL plot of S2 peak under different magnetic field with σ^+ , σ^- or π (linear) excitation.

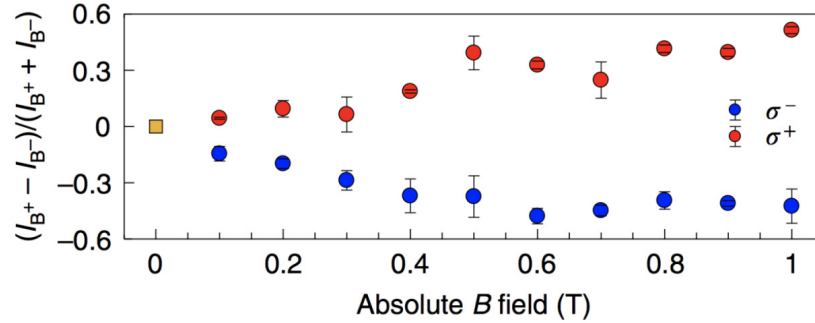


Figure 4.18: The extracted B dependent ratios, $(I_{B^+} - I_{B^-}) / (I_{B^+} + I_{B^-})$ of the S2 red peak.

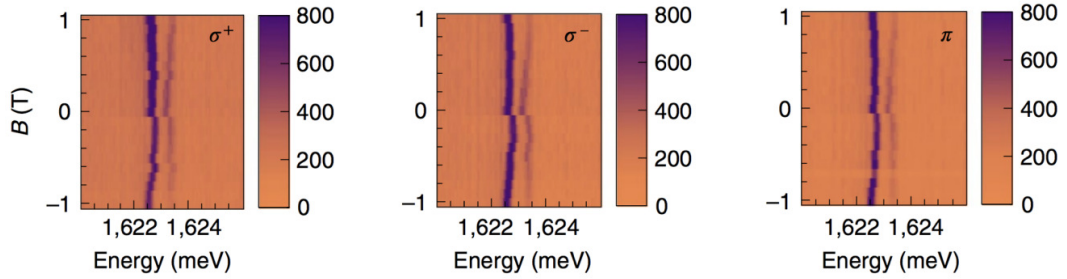


Figure 4.19: PL color plot of D2 doublet with detuning energy similar to laser energy for exciting S2 peak.

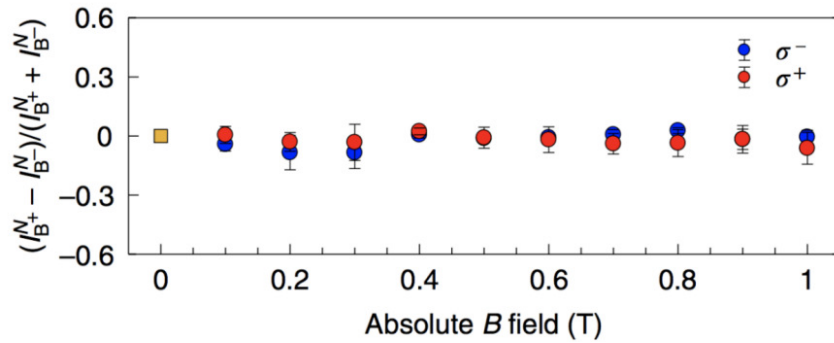


Figure 4.20: B-dependent ratio $(I_{B+}^N - I_{B-}^N)/(I_{B+}^N + I_{B-}^N)$ where I_{B+}^N (I_{B-}^N) denotes the red peak intensity normalized by the intensity sum of the blue and red peaks. Almost no difference between σ^+ or σ^- excitation is observed.

emission of the neutral quantum dot exhibits a similar emission result.

As described above, under a small magnetic field, by controlling the helicity of the excitation, the K_{ex} and $-K_{ex}$ in X_d^+ are selectively excited which combines with a localized hole to form the trion states. This excess hole with an opposite valley compared to K_{ex} or $-K_{ex}$ states can maintain its spin-valley state as long as the X_d^+ survives. Even after the combination of the K_{ex} or $-K_{ex}$ happens which takes a few nanoseconds [29, 31, 44], the hole's spin-valley state is expected to be preserved for a much longer time. The co-polarization between emission and excitation found in X_d^+ state seems similar to the valley polarization of the exciton in TMDs. But the mechanism for these effects is different. For the valley polarization in exciton, the lifetime of the exciton, a

few picoseconds is faster than the valley mixing time of 4 ps assuming exchange energy of 1 meV [34]. However, the PL lifetime of the quantum dot is at the order of nanoseconds and the reason for the helicity-based initialization of a single spin-valley hole is the quenching of exchange interaction. To further corroborate the mechanism, excitation with 33 meV lower energy detuning compared to the D2 neutral dot is used to measure the emission polarization of D2 emission. Figure 4.20 shows negligible emission difference of the two branches in neutral dot D2 under circularly polarized light σ^\pm or linearly polarized light.

4.5 Conclusion and Perspectives

In conclusion, we have observed the single positively charged state X_d^+ and neutral state X_0 at the same QD in monolayer WSe₂. In the single positively charged state, the single spin-valley state of the hole can be selectively initialized by controlling the helicity of the excitation laser under a small perpendicular magnetic field. These results exhibit the robust spin-valley degree in the optically active QDs and provide the platform to exploit the valleytronics in single localized charge carriers. And the optical initialization extends the 2D valleytronics to the level of single spin-valley and provides potential practical applications in quantum information processing.

Chapter 5

Phonon sideband in QD spectra

5.1 Electron-phonon interaction

The Hamiltonian of electron-phonon interaction is assumed to have the form [68]

$$H = H_p + H_e + H_{ei} \quad (5.1)$$

$$H_p = \sum_{\mathbf{q}\lambda} \omega_{\mathbf{q}\lambda} a_{\mathbf{q}\lambda}^+ a_{\mathbf{q}\lambda} \quad (5.2)$$

$$H_e = \sum_i \left[\frac{p_i^2}{2m} + \frac{e^2}{2} \sum_{j \neq i} \frac{1}{r_{ij}} \right] \quad (5.3)$$

$$H_{ei} = \sum_{ij} V(\mathbf{r}_i - \mathbf{R}_j) \quad (5.4)$$

H_p (H_e) describes the phonons (electrons) energy and H_{ei} gives the electron-phonon interaction energy where \mathbf{R}_i (\mathbf{r}_i) is the position of the individual atom i (individual electron i), r_{ij} is the distance between two electrons and $\omega_{\mathbf{q}\lambda}$ is

the phonon energy. Each atom position is oscillating around its equilibrium position $\mathbf{R}_j^{(0)}$ as $\mathbf{R}_j = \mathbf{R}_j^{(0)} + \mathbf{Q}_j$. Therefore, the interaction between electron and phonon can be expanded as

$$V_{ei}(\mathbf{r}_i - \mathbf{R}_j^{(0)} - \mathbf{Q}_j) = V_{ei}(\mathbf{r}_i - \mathbf{R}_j^{(0)}) - \mathbf{Q}_j \cdot \nabla V_{ei}(\mathbf{r}_i - \mathbf{R}_j^{(0)}) + O(Q^2) \quad (5.5)$$

The first term, a constant, and the third term are ignored leaving the electron-phonon interaction as

$$V_{ep}(\mathbf{r}) = \sum_j \mathbf{Q}_j \cdot V_{ei}(\mathbf{r} - \mathbf{R}_j^{(0)}) \quad (5.6)$$

After the Fourier transform for V_{ei}

$$V_{ep}(\mathbf{r}) = \frac{i}{N} \sum_q V_{ei}(\mathbf{q}) e^{i\mathbf{q} \cdot \mathbf{r}} \mathbf{q} \cdot \left(\sum_j \mathbf{Q}_j e^{-i\mathbf{q} \cdot \mathbf{R}_j^{(0)}} \right) \quad (5.7)$$

By using the fact of the displacement \mathbf{Q} in a Fourier transformation

$$\frac{i}{N} \sum_j \mathbf{Q}_j e^{-i\mathbf{q} \cdot \mathbf{R}_j^{(0)}} = \frac{i}{\sqrt{N}} \sum_{\mathbf{G}} \mathbf{Q}_{\mathbf{q}+\mathbf{G}} = - \sum_{\mathbf{G}} \left(\frac{\hbar}{2MN\omega_{\mathbf{q}}} \right)^{1/2} \xi_{\mathbf{q}+\mathbf{G}} (a_{\mathbf{q}} + a_{\mathbf{q}}^+) \quad (5.8)$$

one can obtain the electron-phonon interaction energy as

$$V_{ep}(\mathbf{r}) = - \sum_{\mathbf{q}\mathbf{G}} e^{i\mathbf{r} \cdot (\mathbf{q}+\mathbf{G})} V_{ei}(\mathbf{q} + \mathbf{G}) (\mathbf{q} + \mathbf{G}) \cdot \xi_{\mathbf{q}} \left(\frac{\hbar}{2\rho\nu\omega_{\mathbf{q}}} \right)^{1/2} (a_{\mathbf{q}} + a_{-\mathbf{q}}^+) \quad (5.9)$$

where ρ is the charge density and ν is the volume. The Hamiltonian of electron-phonon interaction is

$$H_{ep} = \int d^3r \rho(\mathbf{r}) V_{ep}(\mathbf{r}) = - \sum_{\mathbf{q}, \mathbf{G}} \rho(\mathbf{q} + \mathbf{G}) V_{ei}(\mathbf{q} + \mathbf{G}) (\mathbf{q} + \mathbf{G}) \cdot \xi_{\mathbf{q}} \left(\frac{\hbar}{2\rho\nu\omega_{\mathbf{q}}} \right)^{1/2} (a_{\mathbf{q}} + a_{-\mathbf{q}}^+) \quad (5.10)$$

For the localized electron, the electron-phonon interaction has three types: deformation potential coupling to acoustic phonons, piezoelectric potential coupling to acoustic phonons and polar coupling to optical phonons. The three interaction types can be written as

1) deformation potential

$$H_{ep} = D \sum_{\mathbf{q}} \left(\frac{\hbar}{2\rho\omega_{\mathbf{q}}\nu} \right)^{1/2} |\mathbf{q}| \rho(\mathbf{q}) (a_{\mathbf{q}} + a_{-\mathbf{q}}^+) \quad (5.11)$$

2) piezoelectric potential

$$H_{ep} = i \sum_{\mathbf{q}} \left(\frac{\hbar}{2\rho\omega_{\mathbf{q}}\nu} \right)^{1/2} M_{\lambda}(\mathbf{q}) \rho(\mathbf{q}) (a_{\mathbf{q}} + a_{-\mathbf{q}}^+) \quad (5.12)$$

3) polar coupling

$$H_{ep} = \sum_{\mathbf{q}} \frac{M}{q\sqrt{\nu}} \rho(\mathbf{q}) (a_{\mathbf{q}} + a_{-\mathbf{q}}^+), \quad M^2 = 2\pi e^2 \hbar \omega_{LO} \left(\frac{1}{\epsilon_{\infty}} - \frac{1}{\epsilon_0} \right) \quad (5.13)$$

A localized quantum dot can be considered as a pair of the localized hole and electron so that one can obtain the phonon-QD interaction by adding hole-phonon and electron-phonon interactions.

5.2 Estimation of the size of QDs

As the QDs have separate energy levels, a phonon bottleneck requires that the transitions process between different QDs states involved with phonons

should at least approximately satisfy the conservation of energy and momentum. However, the virtual transitions called pure dephasing which does not lead to a change of state occupation. This virtual transition process can lead to a non-Lorentzian absorption or emission spectra [69]. In our experiment, the spectra of QDs in monolayer WSe₂ exhibits low energy sidebands. The sidebands are a result of the interaction between the QDs and phonons in the monolayer WSe₂. By studying the sidebands, we can obtain information about the size of quantum dots and phonon-QD interaction form. The phonon-QD interaction model for calculating the emission spectra is the independent boson model [68].

$$H = \hbar\Omega c^+c - \mathbf{M}_0 \cdot \mathbf{E}(c^+d^+ + dc) + \hbar \sum_{j,\mathbf{q}} \omega_j(\mathbf{q}) b_{j,\mathbf{q}}^+ b_{j,\mathbf{q}} + \hbar \sum_{j,\mathbf{q}} (g_{j,\mathbf{q}}^e b_{j,\mathbf{q}} c^+ c - g_{j,\mathbf{q}}^h b_{j,\mathbf{q}} d^+ d + h.c.) \quad (5.14)$$

In this model, the Hamiltonian commutes with c^+c and d^+d implying that the electron and hole numbers are a good quantum number and no relaxation mechanism is involved. Therefore, only the pure dephasing process is considered. The coupling matrix in the Hamiltonian $g_{j,\mathbf{q}}^{e/h} = \zeta_{j,\mathbf{q}}^{e/h} F_{\mathbf{q}}^{e/h}$ can be expressed in two parts, the bulk coupling part and the quantum dot wavefunction part $F_{\mathbf{q}}^{e/h} = \int d^3 |\Psi^{e/h}(\mathbf{r})|^2 e^{i\mathbf{q}\cdot\mathbf{r}}$ The bulk coupling part of the phonon-electron or hole in the three potential types are listed below as

- 1) deformation potential coupling to acoustic phonons

$$\zeta_{AC,j,\mathbf{q}}^{e/h} = \frac{1}{\sqrt{2\rho\hbar\omega_j(q)V}} \quad (5.15)$$

- 2) piezoelectric potential coupling to acoustic phonons

$$\zeta_{AC,j,\mathbf{q}}^{e/h} = i \frac{1}{\sqrt{2\rho\hbar\omega_j(q)V}} M_j(\mathbf{q}) \quad (5.16)$$

3) polar coupling to optical phonons

$$\zeta_{AC,j,\mathbf{q}}^{e/h} = i \left[\frac{2\pi e^2 \omega_{LO}(q)}{\hbar 4\pi} \right]^{1/2} \frac{1}{q} \quad (5.17)$$

Within the independent boson model, it is possible to derive the closed-form analytic expressions for linear signals [68–73]. The complex polarization vector \mathbf{P} to linear order induced by a δ -like laser pulse is shown as

$$\mathbf{P}(t) = \Theta(t) \frac{i|\mathbf{M}_0|^2 \mathbf{E}_0}{\hbar} e^{-i\bar{\Omega}t} \exp\left(\sum_{j,\mathbf{q}} |\gamma|^2 (e^{-i\omega_j(q)t} - n_j(q) |e^{-i\omega_j(q)t} - 1|^2 - 1)\right) =: \epsilon_0 \chi(t) \mathbf{E}_0 \quad (5.18)$$

where $n_j(q) := \frac{1}{e^{\hbar\omega_j(q)/k_b T} - 1}$ represents the equilibrium phonon occupation at temperature T , $\gamma_{j,\mathbf{q}} := (g_{j,\mathbf{q}}^e - \frac{\hbar}{j,\mathbf{q}})/\omega_j(q)$ is a dimensionless coupling strength [69]. $\bar{\Omega} := \Omega - \sum_{j,\mathbf{q}} \omega_j(q) |\gamma_{j,\mathbf{q}}|^2$ stands for the polaron shifted transition frequency [69]. By taking the Fourier transformation for the linear complex polarization, one can obtain the absorption or emission spectral shape.

We utilized the independent boson model and deformation coupling to fit the temperature dependent spectral shapes of QDs in monolayer WSe₂ to obtain the QD size. All the parameters used for monolayer WSe₂ are listed below as $D_e = -6.35$ eV, $D_h = -1.43$ eV [74], $m_K^e = 0.39m_0$, $m_K^v = 0.51m_0$ [75] and $v_{LA} = 3.3 \times 10^5$ cm/s [75].

Quantum dots wavefunction is presented as a two dimensional Gaussian or Lorentzian function and the two choices give similar results. The fitting results with different quantum dot sizes are shown in figure 5.1.

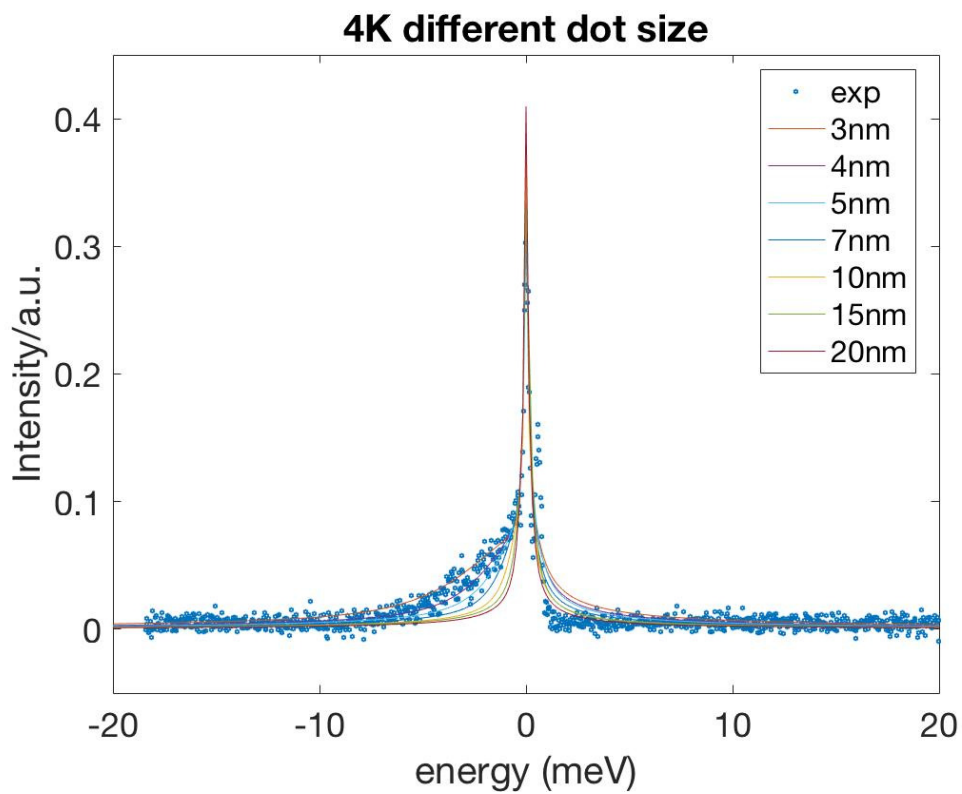


Figure 5.1: Spectral fitting with a size parameter from 3 nm to 20 nm for the red peak of the dot with a phonon sideband. The blue dots are the spectra of the quantum dot. The solid lines are the calculated spectra.

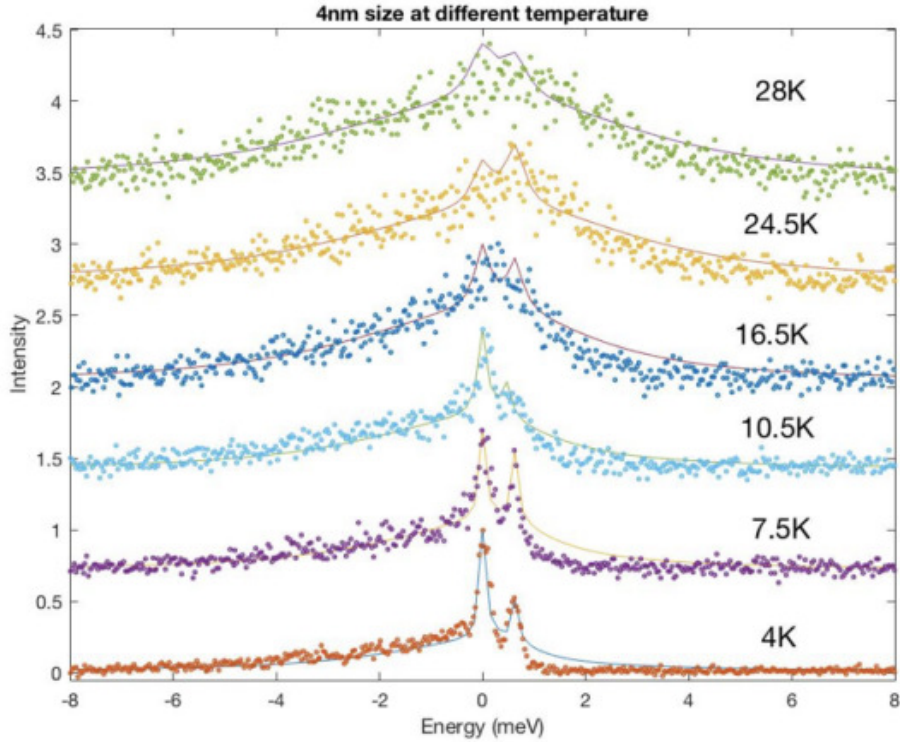


Figure 5.2: Spectral fitting for the doublet quantum dot at different temperatures. The dots are experimental results and the solid lines are the calculated spectra.

The blue dots stand for the experimental spectra of QDs excited by 732.5 nm laser with 400 nW at 4 K. The fitting results of different QD sizes are represented as solid lines. 4 nm result exhibits the best match for low energy sideband.

Next we examine the fitting fidelity with the size parameter of 4 nm at different temperatures shown in figure 5.2. In order to quantify the fitting fidelity, we first calculated the sum of intensity difference between experiment and calculation from -10 meV to 10 meV as well as the intensity sum of the experiment from -10 meV to 10 meV. Then we use the difference between 1 and their ratio to quantify the fidelity of the fitting and the deviation result is shown in figure 5.3. The fidelity is calculated as

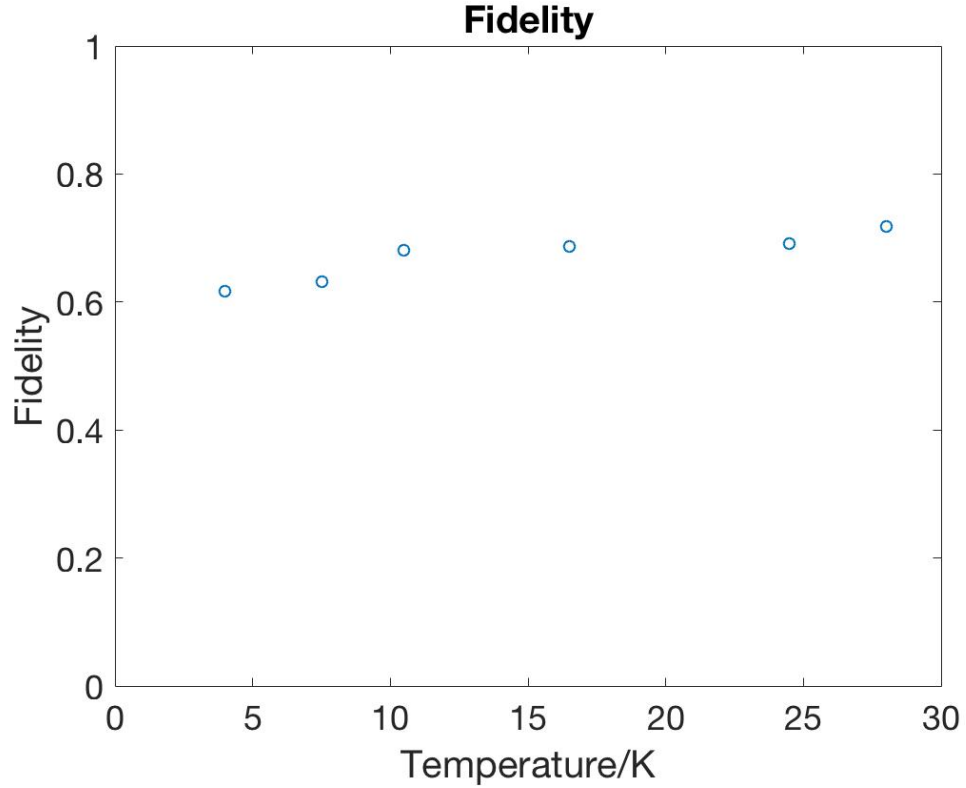


Figure 5.3: Fitting fidelity. The fidelity is about 60-70%.

$$Fidelity = 1 - \frac{\sum_{-10meV \rightarrow 10meV} |I_{experiment} - I_{calculation}|}{\sum_{-10meV \rightarrow 10meV} I_{experiment}} \quad (5.19)$$

The fidelity for all temperatures is around 60% to 70%. One source of the deviation is the intensity difference at high energy sidebands. Our experiment result exhibits negligible intensity from 1 meV to 3 meV but the calculation result has intensity in this region. The difference is especially apparent at low temperatures from 4 to 10 K which needs more research in the future.

5.3 Conclusion and Perspectives

Our results show QDs intrinsic properties of the coupling type and the QD size of about 4 nm. The deformation coupling between QDs and acoustic phonons provides a good fitting for the spectra of QD with a phonon sideband and the fitting fidelity is about 60% to 70%. Its size is larger than the Bohr radius of the exciton in monolayer WSe₂ which is different from the QD in GaAs. Further study can address the phonon sideband at the high energy part to improve the fitting fidelity of the QDs spectra.

Bibliography

- [1] Novoselov, K. S. et al. Electric field effect in atomically thin carbon films. *Science* 306, 666669 (2004).
- [2] Novoselov, K. S. et al. Two-dimensional atomic crystals. *Proc. Natl Acad. Sci. USA* 102, 1045110453 (2005).
- [3] Schaibley, J. R., H. Yu, G. Clark, P. Rivera, J. S. Ross, K. L. Seyler, W. Yao, and X. Xu, Valleytronics in 2D materials, *Nat. Rev. Mater.* 1, 16055,2016.
- [4] Liu, G.-B.; Xiao, D.; Yao, Y.; Xu, X.; Yao, W. Electronic Structures and Theoretical Modelling of Two-Dimensional Group-VIB Transition Metal Dichalcogenides. *Chem. Soc. Rev.* 2015, 44, 2643 2663.
- [5] Gorbachev, R. et al. Detecting topological currents in graphene superlattices. *Science* 346, 448451 (2014). The first experimental report of valley Hall effect in graphene with broken inversion symmetry, using an electronic transport measurement.
- [6] Sui, M. et al. Gate-tunable topological valley transport in bilayer graphene. *Nat. Phys.* 11, 10271031 (2015).

- [7] Shimazaki, Y. et al. Generation and detection of pure valley current by electrically induced Berry curvature in bilayer graphene. *Nat. Phys.* 11, 10321036 (2015).
- [8] Mak, K. F., McGill, K. L., Park, J. & McEuen, P. L. The valley Hall effect in MoS₂ transistors. *Science* 344, 14891492 (2014).
- [9] Lee, J., Mak, K. F. & Shan, J. Electrical control of the valley Hall effect in bilayer MoS₂ transistors. *Nat. Nanotechnol.* 11, 421425 (2016).
- [10] Le D, Barinov A., Preciado E., Isarraraz M., Tanabe I., Komesu T., Troha C., Bartels L., Rahman T. S. and Dowben P. A. Spinorbit coupling in the band structure of monolayer WSe₂. *Journal of Physics: Condensed Matter*, 2015, 27, 182201.
- [11] S.-W. Yu, T. Lischke, R. David, N. Muller, U. Heinzmann, C. Pettenkofer, A. Klein, A.Ya. Perlov, E.E. Krasovskii, W. Schattke, J. Braun, Spin resolved photoemission spectroscopy on WSe₂, *Journal of Electron Spectroscopy and Related Phenomena* 101103 (1999) 449454.
- [12] Riley, J. M. et al. Direct observation of spin-polarized bulk bands in an inversion-symmetric semiconductor. *Nat. Phys.* 10, 835839 (2014).
- [13] Mak, K. F., He, K., Shan, J. & Heinz, T. F. Control of valley polarization in monolayer MoS₂ by optical helicity. *Nature Nanotech.* 7, 494498 (2012).
- [14] Xiao, D., Liu, G-B., Feng, W., Xu, X. & Yao, W. Coupled spin and valley physics in monolayers of MoS₂ and other Group-VI dichalcogenides. *Phys. Rev. Lett.* 108, 196802 (2012).

- [15] Chernikov, A. et al. Exciton binding energy and nonhydrogenic Rydberg series in monolayer WS_2 . *Phys. Rev. Lett.* 113, 076802 (2014).
- [16] Zhu, B., Chen, X. & Cui, X. Exciton binding energy of monolayer WS_2 . *Sci. Rep.* 5, 9218 (2015).
- [17] Ye, Z. et al. Probing excitonic dark states in single-layer tungsten disulfide. *Nature* 513, 214218 (2014).
- [18] He, K. et al. Tightly bound excitons in monolayer WSe_2 . *Phys. Rev. Lett.* 113, 026803 (2014).
- [19] Cheiwchanchamnangij, T. & Lambrecht, W. R. L. Quasiparticle band structure calculation of monolayer, bilayer, and bulk MoS_2 . *Phys. Rev. B* 85, 205302 (2012).
- [20] Hanbicki, A. T., Currie, M., Kioseoglou, G., Friedman, A. L. & Jonker, B. T. Measurement of high exciton binding energy in the monolayer transition-metal dichalcogenides WS_2 and WSe_2 . *Solid State Commun.* 203, 1620 (2015).
- [21] Nihit Saigal, Vasam Sugunakar, and Sandip Ghosha, Exciton binding energy in bulk MoS_2 : A reassessment. *Appl. Phys. Lett.* 108, 132105 (2016).
- [22] S. B. Nam, D. C. Reynolds, C. W. Litton, R. J. Almassy, T. C. Collins, and C. M. Wolfe, Free-exciton energy spectrum in GaAs. *Phys. Rev. B.* 13, 761 (1976).
- [23] Qiu, D. Y., Felipe, H. & Louie, S. G. Optical spectrum of MoS_2 : many-body effects and diversity of exciton states. *Phys. Rev. Lett.* 111, 216805 (2013).

- [24] Feng, J., Qian, X., Huang, C. W. & Li, J. Strain-engineered artificial atom as a broad-spectrum solar energy funnel. *Nat. Photonics* 6, 866872 (2012).
- [25] Berkelbach, T. C., Hybertsen, M. S. & Reichman, D. R. Theory of neutral and charged excitons in monolayer transition metal dichalcogenides. *Phys. Rev. B* 88, 045318 (2013).
- [26] Zhang, C., Wang, H., Chan, W., Manolatou, C. & Rana, F. Absorption of light by excitons and trions in monolayers of metal dichalcogenide MoS_2 : experiments and theory. *Phys. Rev. B* 89, 205436 (2014).
- [27] Steinhoff, A., Rosner, M., Jahnke, F., Wehling, T. O. & Gies, C. Influence of excited carriers on the optical and electronic properties of MoS_2 . *Nano Lett.* 14, 37433748 (2014).
- [28] Tongay, S. et al. Defects activated photoluminescence in two-dimensional semiconductors: interplay between bound, charged, and free excitons. *Sci. Rep.* 3, 2657 (2013).
- [29] Srivastava, A. et al. Optically active quantum dots in monolayer WSe_2 . *Nat. Nanotech.* 10, 491496 (2015).
- [30] Branny, A., Kumar, S., Proux, R. & Gerardot, B. D. Deterministic strain-induced arrays of quantum emitters in a two-dimensional semiconductor. *Nat. Commun.* 8, 15053 (2017).
- [31] Koperski, M. et al. Single photon emitters in exfoliated WSe_2 structures. *Nat. Nanotech.* 10, 503506 (2015).

- [32] Chakraborty, C., Kinnischtzke, L., Goodfellow, K. M., Beams, R. & Vamvakas, A. N. Voltage controlled quantum light from an atomically thin semiconductor. *Nat. Nanotech.* 10, 507511 (2015).
- [33] Hsu, W.-T. et al. Optically initialized robust valley- polarized holes in monolayer WSe₂. *Nat. Commun.* 6, 8963 (2015).
- [34] Yu, H., Liu, G.-B., Gong, P., Xu, X. & Yao, W. Dirac cones and Dirac saddle points of bright excitons in monolayer transition metal dichalcogenides. *Nat. Commun.* 5, 3876 (2014).
- [35] Glazov, M. M. and Amand, T. and Marie, X. and Lagarde, D. and Bouet, L. & Urbaszek, B. Exciton fine structure and spin decoherence in monolayers of transition metal dichalcogenides. *Phys. Rev. B.* 89, 201302 (2014).
- [36] Wang, Gang and Chernikov, Alexey and Glazov, Mikhail M. and Heinz, Tony F. and Marie, Xavier and Amand, Thierry and Urbaszek, Bernhard. Colloquium: Excitons in atomically thin transition metal dichalcogenides. *Rev. Mod. Phys.* 90. 021001 (2018).
- [37] Ali Jawaid, Dhriti Nepal, Kyoungweon Park, Michael Jespersen, Anthony Qualley, Peter Mirau, Lawrence F. Drummy, and Richard A. Vaia. Mechanism for Liquid Phase Exfoliation of MoS₂. *Chem. Mater.*, 2016, 28 (1), 337348.
- [38] Lee, Y. H., Zhang, X. Q., Zhang, W., Chang, M. T., Lin, C. T., Chang, K. D., Yu, Y. C., Wang, J. T. W., Chang, C. S., Li, L. J. and Lin, T. W. (2012), Synthesis of Large-Area MoS₂ Atomic Layers with Chemical Vapor Deposition. *Adv. Mater.*, 24: 23202325.

- [39] Castellanos-Gomez, A. et al. Deterministic transfer of two-dimensional materials by all-dry viscoelastic stamping. *2D Mater.* 1, 011002 (2014).
- [40] Dean, C., Young A., Meric, I., Lee, C., Wang L., Sorgenfrei S., Watanabe K., Taniguchi T., Kim P., Shepard K. Boron nitride substrates for high-quality graphene electronics. *Nature Nanotechnology* 2010, 5, 722-726.
- [41] Sidler, M. et al. Fermi polaron-polaritons in charge-tunable atomically thin semiconductors. *Nat. Phys.* 13, 255261 (2016).
- [42] Gammon, D., Snow, E. S., Shanabrook, B. V., Katzer, D. S. & Park, D. Fine structure splitting in the optical spectra of single GaAs quantum dots. *Phys. Rev. Lett.* 76, 30053008 (1996).
- [43] Tonndorf, P. et al. Single-photon emission from localized excitons in an atomically thin semiconductor. *Optica* 2, 347352 (2015).
- [44] He, Y.-M. et al. Single quantum emitters in monolayer semiconductors. *Nat. Nanotech.* 10, 497502 (2015).
- [45] Luo, X. et al. Effects of lower symmetry and dimensionality on Raman spectra in two-dimensional 152 WSe_2 . *Phys. Rev. B* 88, 195313 (2017).
- [46] Heitz, R., Mukhametzhanov, I., Stier, O., Madhukar, A. & Bimberg, D. Enhanced polar exciton-LO-phonon interaction in quantum dots. *Phys. Rev. Lett.* 83, 46544657 (1999). 37 Hecht, E. and Zajac, A. *Optics* Addison-Wesley, Reading, MA, Sec. 8.12 (1974).
- [47] Zhang, L. & Niu, Q. Chiral phonons at high-symmetry points in monolayer hexagonal lattices. *Phys. Rev. Lett.* 115, 115502 (2015).

- [48] Zhang, L. & Niu, Q. Angular Momentum of Phonons and the Einstein–de Haas Effect. *Phys. Rev. Lett.* 112, 085503 (2014).
- [49] Zhu, H. et al. Observation of chiral phonons. *Science* 359, 579582 (2018).
- [50] Cai, Y., Lan, J., Zhang, G. & Zhang, Y.-W. Lattice vibrational modes and phonon thermal conductivity of monolayer MoS₂. *Phys. Rev. B* 89, 035438 (2014).
- [51] Wang, G. et al. Giant Enhancement of the Optical Second-Harmonic Emission of WSe₂ Monolayers by 158 Laser Excitation at Exciton Resonances. *Phys. Rev. Lett.* 114, 1097403 (2015).
- [52] Imamoglu, A. et al. Quantum information processing using quantum dot spins and cavity-QED. *Phys. Rev. Lett.* 83, 42044207 (1999). 46
- [53] Giovannetti, V., Lloyd, S. & Maccone, L. Advances in quantum metrology. *Nat. Photon.* 5, 222229 (2011).
- [54] Palacios-Berraquero, C. et al. Large-scale quantum-emitter arrays in atomically thin semiconductors. *Nat. Commun.* 8, 15093 (2017).
- [55] Schwarz, S. et al. Electrically pumped single-defect light emitters in WSe₂. *2D Mater.* 3, 025038 (2016).
- [56] Stier, A. V., McCreary, K. M., Jonker, B. T., Kono, J. & Crooker, S. A. Exciton diamagnetic shifts and valley Zeeman effects in monolayer WS₂ and MoS₂ to 65 tesla. *Nat. Commun.* 7, 10643 (2016).
- [57] Courtade, E. et al. Charged excitons in monolayer WSe₂: experiment and theory. *Phys. Rev. B* 96, 085302 (2017).

- [58] Jiang, C. et al. Microsecond dark-exciton valley polarisation memory in two-dimensional heterostructures. *Nat. Commun.* 9, 753 (2018).
- [59] Yang, L. et al. Long-lived nanosecond spin relaxation and spin coherence of electrons in monolayer MoS₂ and WS₂. *Nat. Phys.* 11, 830834 (2015).
- [60] Dey, P. et al. Gate-controlled spin-valley locking of resident carriers in WSe₂ monolayers. *Phys. Rev. Lett.* 119, 137401 (2017).
- [61] Kim, J. et al. Observation of ultralong valley lifetime in WSe₂/MoS₂ heterostructures. *Sci. Adv.* 3, e1700518 (2017).
- [62] Yan, T., Yang, S., Li, D. & Cui, X. Long valley relaxation time of free carriers in monolayer WSe₂. *Phys. Rev. B* 95, 241406 (2017).
- [63] Chakraborty, C. et al. 3D localised trions in monolayer WSe₂ in a charge 2 tuneable van der Waals heterostructure. *Nano Lett.* 18, 28592863 (2018).
- [64] Srivastava, A. et al. Valley Zeeman effect in elementary optical excitations of monolayer WSe₂. *Nat. Phys.* 11, 141147 (2015).
- [65] Aivazian, G. et al. Magnetic control of valley pseudospin in monolayer WSe₂. *Nat. Phys.* 11, 148152 (2015).
- [66] MacNeill, D. et al. Breaking of valley degeneracy by magnetic field in monolayer MoSe₂. *Phys. Rev. Lett.* 114, 037401 (2015).
- [67] Li, Y. et al. Valley splitting and polarisation by the Zeeman effect in monolayer MoSe₂. *Phys. Rev. Lett.* 113, 266804 (2014).
- [68] G. Mahan, *Many-Particle Physics* Plenum, New York, 1990.
- [69] B. Krummheuer, V. M. Axt, and T. Kuhn, *Phys. Rev. B* 65, 195313 (2002).

- [70] C.B. Duke and G.D. Mahan, Phys. Rev. 139, A1965 1965.
- [71] V.M. Axt, M. Herbst, and T. Kuhn, Superlattices Microstruct. 26, 117 1999.
- [72] D. Steinbach, G. Kocherscheidt, M. U. Wehner, H. Kalt, M. Wegener, K. Ohkawa, D. Hommel, and V. M. Axt, Phys. Rev. B 60, 12 079 1999.
- [73] H. Castella and R. Zimmermann, Phys. Rev. B 59, R7801 1999.
- [74] Wiktor, J.; Pasquarello, A. Absolute Deformation Potentials of Two-Dimensional Materials. Phys. Rev. B: Condens. Matter Mater. Phys. 2016, 94, 18.
- [75] Z. Jin, X. Li, J. T. Mullen, and K. W. Kim, Intrinsic transport properties of electrons and holes in monolayer transition-metal dichalcogenides, Phys. Rev. B 90, 045422 (2014).
- [76] Chen, S.-Y., Zheng, C., Fuhrer, M. S. & Yan, J. Helicity-resolved Raman scattering of MoS₂, MoSe₂, WS₂, and WSe₂ atomic layers. Nano. Lett. 15, 25262532 (2015).
- [77] Drapcho, S. G. et al. Apparent breakdown of Raman selection rule at valley exciton resonances in monolayer MoS₂. Phys. Rev. B 95, 165417 (2017).
- [78] Yoshikawa, N., Tani, S. & Tanaka, K. Raman-like resonant secondary emission causes valley coherence in CVD-grown monolayer MoS₂. Phys. Rev. B 95, 115419 (2017).
- [79] Cao, T. et al. Valley-selective circular dichroism of monolayer molybdenum disulphide. Nature Commun. 3, 887 (2012).

- [80] Zeng, H., Dai, J., Yao, W., Xiao, D. & Cui, X. Valley polarization in MoS₂ monolayers by optical pumping. *Nature Nanotech.* 7, 490493 (2012).
- [81] Xu, X., Yao, W., Xiao, D. & Heinz, T. F. Spin and pseudospins in layered transition metal dichalcogenides. *Nat. Phys.* 10, 343350 (2014).
- [82] Jones, A. M. et al. Optical generation of excitonic valley coherence in monolayer WSe₂. *Nature Nanotech.* 8, 634638 (2013).
- [83] Lagarde, D. et al. Carrier and polarization dynamics in monolayer MoS₂. *Phys. Rev. Lett.* 112, 047401 (2014).
- [84] Bayer, M. et al. Fine structure of neutral and charged excitons in self-assembled In(Ga)As/(Al)GaAs quantum dots. *Phys. Rev. B* 65, 195315 (2002).
- [85] Mak, K. F., Lee, C., Hone, J., Shan, J. & Heinz, T. F. Atomically thin MoS₂: a new direct-gap semiconductor. *Phys. Rev. Lett.* 105, 136805 (2010).
- [86] Splendiani, A. et al. Emerging photoluminescence in monolayer MoS₂. *Nano Lett.* 10, 12711275 (2010).